ASSESSMENT OF THE EFFECT OF VAPOR FLOW ON THE THERMAL PERFORMANCE OF A FLAT GROOVED HEAT PIPE

A THESIS SUBMITTED TO
THE GRADUATE SCHOOL OF NATURAL AND APPLIED SCIENCES
OF
MIDDLE EAST TECHNICAL UNIVERSITY

BY

BESTE DEREBAŞI

IN PARTIAL FULFILLMENT OF THE REQUIREMENTS
FOR
THE DEGREE OF MASTER OF SCIENCE
IN
MECHANICAL ENGINEERING

JUNE 2023

Approval of the thesis:

ASSESSMENT OF THE EFFECT OF VAPOR FLOW ON THE THERMAL PERFORMANCE OF A FLAT GROOVED HEAT PIPE

submitted by **BESTE DEREBAŞI** in partial fulfillment of the requirements for the degree of **Master of Science in Mechanical Engineering Department, Middle East Technical University** by,

Prof. Dr. Halil Kalıpçılar
Dean, Graduate School of **Natural and Applied Sciences** _____

Prof. Dr. M. A. Sahir Arıkan
Head of Department, **Mechanical Engineering** _____

Prof. Dr. Zafer Dursunkaya
Supervisor, **Mechanical Engineering, METU** _____

Assoc. Prof. Dr. Barbaros Çetin
Co-supervisor, **Mechanical Engineering, Bilkent University** _____

Examining Committee Members:

Prof. Dr. Almıla Güvenç Yazıcıoğlu
Mechanical Engineering, METU _____

Prof. Dr. Zafer Dursunkaya
Mechanical Engineering, METU _____

Assoc. Prof. Dr. Barbaros Çetin
Mechanical Engineering, Bilkent University _____

Assoc. Prof. Dr. Özgür Bayer
Mechanical Engineering, METU _____

Assist. Prof. Dr. Altuğ Özçelikkale
Mechanical Engineering, METU _____

Date:19.06.2023

I hereby declare that all information in this document has been obtained and presented in accordance with academic rules and ethical conduct. I also declare that, as required by these rules and conduct, I have fully cited and referenced all material and results that are not original to this work.

Name, Surname: Beste Derebaşı

Signature :

ABSTRACT

ASSESSMENT OF THE EFFECT OF VAPOR FLOW ON THE THERMAL PERFORMANCE OF A FLAT GROOVED HEAT PIPE

Derebaşı, Beste
M.S., Department of Mechanical Engineering
Supervisor: Prof. Dr. Zafer Dursunkaya
Co-Supervisor: Assoc. Prof. Dr. Barbaros Çetin

June 2023, 83 pages

Flat grooved heat pipe (FGHP) is widely employed in various applications such as cooling components in electronics due to their high heat transfer capability and reliability. As electronic devices continue to evolve towards more compact designs, the demand for thinner FGHP is becoming thinner to provide compatible thermal management. This study extends a recently developed modeling tool by incorporating vapor flow and interfacial effects between the two phases of the working fluid in FGHP. The model is validated with varying vapor space thickness, resulting in an improved representation of the free surface geometry. The thermal performance of FGHP is evaluated by subjecting the model to different vapor space thicknesses. It is observed that reducing the vapor space thickness leads to a decrease in the maximum heat-carrying capacity of FGHP while enhancing the evaporation performance. Furthermore, experimental investigations are conducted to validate the numerical findings, involving varying filling ratios and heat loads for each vapor space thickness.

Keywords: Heat pipe modeling, flat-grooved heat pipes, liquid-vapor flow interaction, two-phase immiscible flows, evaporation enhancement

ÖZ

BUHAR AKIŞININ OLUKLU ISI BORUSUNUN ISIL PERFORMANSI ÜZERİNDEKİ ETKİSİ

Derebaşı, Beste
Yüksek Lisans, Makina Mühendisliği Bölümü
Tez Yöneticisi: Prof. Dr. Zafer Dursunkaya
Ortak Tez Yöneticisi: Doç. Dr. Barbaros Çetin

Haziran 2023 , 83 sayfa

Oluklu ısı boruları, yüksek ısıl performansı ve güvenilirlikleri nedeniyle sıklıkla elektronik cihazlarının soğutmasında kullanılmaktadır. Bu tez çalışmasında, düz oluklu ısı borularının tasarımı için geliştirilen modele, sıvı ve buhar fazları arasındaki etkileşimi ve buhar akışı eklenmiştir. Model, literatürdeki farklı çalışmalar ile doğrulanmıştır ve modele buhar akışının dahil edilmesiyle sıvı-buhar arasındaki yüzey geometrisinde gerçeğe daha yakın sonuçlar elde edildiği gözlenmiştir. Ek olarak, model ısıl performans üzerindeki etkileri değerlendirmek için farklı buhar boşluk kalınlıklarıyla test edilmiştir. Buhar boşluk kalınlığının azaltılmasının, FGHP'nin maksimum taşıma ısı kapasitesini azalttığı ve buharlaşma performansını artırdığı tespit edilmiştir. Sayısal çalışmanın yanı sıra, her bir buhar boşluk kalınlığı için farklı doldurma oranları ve ısı yükleri altında deneysel çalışmalar gerçekleştirilmiştir.

Anahtar Kelimeler: oluklu ısı boruları, gaz akışı, sıvı-gaz etkileşimi, iki fazlı karışmayan akışlar, buharlaştırma iyileştirmesi

To my grandmother

ACKNOWLEDGMENTS

I would like to express my sincere acknowledgment to my supervisor, Prof. Dr. Zafer Dursunkaya who always made me feel like a teammate. His motivation and wisdom inspired me in every meeting, I am grateful for all of them, not only those in the academic field. I would also like to extend my deepest gratitude to my co-advisor Assoc. Prof. Dr. Barbaros Çetin for his valuable constructing comments and guidance.

I would like to acknowledge Dr. Samet Saygan for his endless help. Also, I want to thank Mr. Mustafa Yalçın for his technical, and psychological support throughout my education.

I owe thanks to my family, Fadime Uysal, Mustafa Derebaşı, Kadriye Derebaşı, Hatice Köse, and Oğuz Köse for their endless support and for believing in me. I want to express my gratefulness to my dears, Bengisu Derebaşı, Yusuf Köse, Günce Köse who are always there with me in the back seat of the car.

I would like to express my special thanks to Eylül Gedik, who is and will be my companion. I also want to acknowledge my friends Deniz Değirmenci, Elif Aslan, Alperen Alparslan, Can Koç, Sıla Yüksel, Ayça Çark, Talat Acar, Mohsen Oskouei, Ramazan Doğanay, Elyas Bakhsh, Pelin Çağlayan for their valuable encouragements, and helps.

Lastly, I would like to thank Turkish Scientific and Technical Research Council (TÜBİTAK) for the financial support during my M.Sc. education.

TABLE OF CONTENTS

ABSTRACT v

ÖZ vi

ACKNOWLEDGMENTS viii

TABLE OF CONTENTS ix

LIST OF TABLES xii

LIST OF FIGURES xiii

LIST OF ABBREVIATIONS xvi

LIST OF SYMBOLS xvii

CHAPTERS

1 INTRODUCTION 1

1.1 Heat Pipe Classification 3

1.1.1 Conventional Capillary Driven Heat Pipes 4

1.1.2 Pulsating Heat Pipes 4

1.1.3 Loop Heat Pipes 5

1.1.4 Micro Heat Pipes 5

1.2 Definitions 6

1.2.1 Surface Tension 6

1.2.2 Dry-out . . . 7
1.2.3 Working Fluid Selection . . . 7
1.2.4 Filling Ratio . . . 7
1.2.5 HP Performance Indicators . . . 8
1.3 Literature Review . . . 9
1.3.1 Numerical studies . . . 9
1.3.2 Experimental studies . . . 16
1.4 Objective and Outline of Study . . . 20
2 METHODOLOGY . . . 21
2.1 Numerical Modeling . . . 21
2.1.1 Flow Model . . . 24
2.1.2 Thermal Analysis . . . 29
2.2 Experimental Work . . . 32
2.2.1 Experimental Preparation . . . 33
2.2.1.1 Thermocouple Calibration . . . 34
2.2.2 Experimental Procedure . . . 35
2.2.3 Vapor Flow Experiments . . . 36
2.2.4 Silicon FGHP Experiments . . . 38
3 RESULTS . . . 41
3.1 Numerical Model Validation . . . 41
3.1.1 Validation with the Model without Vapor Flow . . . 41
3.1.2 Validation of the Effect of Vapor Spacing . . . 44
3.2 Simulation Results of Varying Vapor Space Thicknesses . . . 49

3.3 Vapor Flow Experiment Results 55

3.3.1 Experiments with 2 mm Vapor Space Thickness FGHP 67

4 CONCLUSION 71

REFERENCES 75

LIST OF TABLES

TABLES

Table 1.1 Advantages and disadvantages of wick types 3

Table 1.2 Summary of some studies accounting for the terms in the momentum balance of the liquid control volume (Adapted from) 16

Table 2.1 Measured pressures inside the FGHP 34

Table 2.2 Simulation results of wall temperature difference range for different vapor space thicknesses at different heat loads 36

Table 2.3 Elevation of working fluid measurements at different filling ratios experimented on FGHP with $h_v = 2\ \mathrm{mm}$ 38

Table 2.4 Operating and geometrical specifications Si FGHP experiments . . . 39

Table 3.1 Operating and geometrical specifications of FGHP for validation study 42

Table 3.2 Operational parameters and geometrical specifications 44

Table 3.3 Operating and geometrical specifications of FGHP configuration for vapor flow experiments 55

Table 3.4 Experimental and numerical model results under different heat loads for $h_v = 3\ \mathrm{mm}$ and $h_v = 6\ \mathrm{mm}$ 63

Table 3.5 Numerical and experimental results of ΔT_{wall} for $h_v = 3\ \mathrm{mm}$ and $h_v = 6\ \mathrm{mm}$ under various heat loads 66

LIST OF FIGURES

FIGURES

Figure 1.1 Heat pipe working mechanism 2

Figure 1.2 Different wick types (a) screen mesh (b) groove (c) sinter 3

Figure 1.3 Schematic of pulsating heat pipes 4

Figure 1.4 Different cross-sections of MHPs 5

Figure 1.5 Control volume 15

Figure 2.1 Flow chart of the solution procedure 23

Figure 2.2 Physical domain of vapor and liquid flows 24

Figure 2.3 Boundary conditions for analytical solution of vapor and liquid domains 26

Figure 2.4 Thermal resistance network 30

Figure 2.5 Schematic of thermal resistance and circuit representation for evaporator and condenser sections 31

Figure 2.6 Experimental setup 32

Figure 2.7 Components of FGHP assembly 33

Figure 2.8 HP assembly for charging the working fluid 35

Figure 2.9 Copper-IPA material contact angle measurement 36

Figure 2.10 FGHP schematic showing the vapor space thickness 37

Figure 2.11 Schematics of geometrical parameters of FGHP 39

Figure 2.12 Wall temperature variation on Si FGHP for varying filling ratios . 40

Figure 2.13 Condensation on the top frame 40

Figure 3.1 Validation with the model that excludes the gas flow effect at 9.5 W heat load: (a) radius of curvature distribution, (b) wall temperature distribution 43

Figure 3.2 Temperature distribution under $7.5\ \mathrm{Wcm^{-2}}$ heat rate for $h_v = 2\,\mathrm{mm}$ 45

Figure 3.3 Experimental and numerical study comparison for $h_v = 2$ mm and $h_v = 1$ mm (dashed lines represent the numerical results for $h_v = 2$ mm) 46

Figure 3.4 Radius of curvature distribution results of the current study, the model developed by Saygan not including the vapor flow (dashed lines), experimental data (a) $h_v = 1$ mm, (b) $h_v = 2$ mm 48

Figure 3.5 (a) Edge angle variation, (b) variation of curvature along the FGHP for varying vapor space thicknesses 50

Figure 3.6 (a) Wall temperature distribution, (b) wall temperature difference and q_{ratio}, for varying vapor space thicknesses 51

Figure 3.7 Velocity and shear stress distributions at the interface (a) U_{int}, (b) τ_{int} 53

Figure 3.8 Liquid axial velocity contour in x–y plane at middle section of FGHP (a) $h_v = 1$ mm, (b) $h_v = 5$ mm 54

Figure 3.9 ΔT_{wall} results of $h_v = 3$ mm under different heat loads: (a) experimental results for varying filling ratios, (b) numerical results for varying θ_{beg} 57

Figure 3.10 Boundary and matching conditions of unidirectional condensation model on the fin top 58

Figure 3.11 Experimental and numerical results of wall temperature distribution for $h_v = 3$ mm at 7.0 W heat load 59

Figure 3.12 Experimental and numerical results of ΔT_{wall} at the operating range of $h_v = 3$ mm FGHP for varying heat inputs 60

Figure 3.13 Dry-out region taken at different periods of the experiment: (a) 30 min (dry region is 19 mm), (b) 1 hour (dry region is 27 mm), (c) 2 hours (dry region is 38 mm) 61

Figure 3.14 Experimental results of ΔT_{wall} for varying filling ratios for $h_v = 6$ mm under different heat inputs 62

Figure 3.15 T_{wall} variation along the FGHP with 4, 7 and 9 W heat inputs: (a) $h_v = 3$ mm, (b) $h_v = 6$ mm 64

Figure 3.16 Experimental results of ΔT_{wall} with varying filling ratios with 7, 9, 10, 11, 12 and 13 W for: (a) $h_v = 3$ mm, (b) $h_v = 6$ mm 65

Figure 3.17 Experimental and numerical results of ΔT_{wall} for $h_v = 2$ mm under 4.0, 5.5, 7.0 W 68

Figure 3.18 Examples of transient behavior at 7 W heat load for: (a) $h_v = 2$ mm, (b) $h_v = 6$ mm 69

LIST OF ABBREVIATIONS

2D	2 Dimensional
3D	3 Dimensional
CV	Control volume
FGHP	Flat grooved heat pipe
FR	Filling ratio
HP	Heat pipe
MHP	Micro heat pipe
VC	Vacuum chamber

LIST OF SYMBOLS

h	height, mm
L	Length, m
p	Pressure, Pa
Q	Heat input, W
R	Thermal resistance, $\mathrm{K/W}$
$\mathcal{R}$	Radius of curvature, mm
T	Temperature, $^{\circ}\mathrm{C}$
U	Velocity in axial direction, $\mathrm{m/s}$
V	Volume, m^3
w	width, mm
x	x-direction
y	y-direction
z	z-direction
	Greek Symbols
α	Contact angle, $^{\circ}$
θ	Edge angle, $^{\circ}$
κ	Curvature, $1/\mathrm{m}$
μ	Dynamic viscosity, $\mathrm{Pa \cdot s}$
ρ	Density, $\mathrm{kg/m}^3$
σ	Surface tension, $\mathrm{N/m}$
τ	Shear stress, Pa

Subscripts

a	adiabatic
ax	axial
b	base
beg	beginning
c	condenser
ca	material contact angle
e	evaporator
f	fin
g	groove
in	input
int	interface
l	liquid
pc	phase change
v	vapor
$wall$	wall

CHAPTER 1

INTRODUCTION

Advances in electronics increase the complexities and the number of elements in electronic systems. One of the main components the transistor, which is made of semiconductor material, is used as a power and signal amplifier. The number of transistors is an indicator of the complexity level of an electronic system. The 2022 design of the Apple M1 Ultra illustrates its complexity as it contains 114 billion transistors while Apple A7 has 1 billion transistors in 2013 [1]. These improvements result in an increase in power requirements; moreover, up to 80% of the power consumption is dissipated by heat which causes the increased temperature of the components if not removed. A temperature increase of components expedites the aging of semiconductor constituents and conduces performance deterioration. To illustrate, a 27% drop in working efficiency of semiconductor crystals is observed when the temperature is increased from $25°$C to $75°$C [2]. In addition to the increasing complexities in electronics, components become smaller, and more heat should be dissipated in smaller areas. Therefore, natural convection becomes insufficient as a cooling mechanism. The other options such as forced convection with air/liquid, thermo-electric cooling units, etc. have limited usage due to larger space and power requirements and reliability. Heat pipes (HP) are a type of passive thermal management device that were first proposed by Gaugler in 1944. However, its physics was not fully explained. Then in 1963, Grover conducted experiments on HP for space program applications [3]. It was Grover who gave the device its name "heat pipe" [4]. Since then, the concept of HPs has been extensively studied and applied in various contexts. In addition to their usage in electronics cooling, HPs have begun to be an element of clean energy systems such as solar and geothermal power plants due to their ability to convert the available energy to use without the need for an external power supply [5].

Heat pipes are highly effective in heat transfer in a passive manner since the phase change mechanism is involved. They can transmit high heat loads within a low-temperature difference even at longer distances. HP can reach more than 10-fold of the bare solid material of HP in terms of effective thermal conductivity [4].

These devices consist of 3 physical domain which is an outer wall, capillary structure, and liquid and vapor domain. HPs have 3 sections which are the evaporator, condenser, and adiabatic section. A schematic of the working principle and the domains are presented in Fig. 1.1.

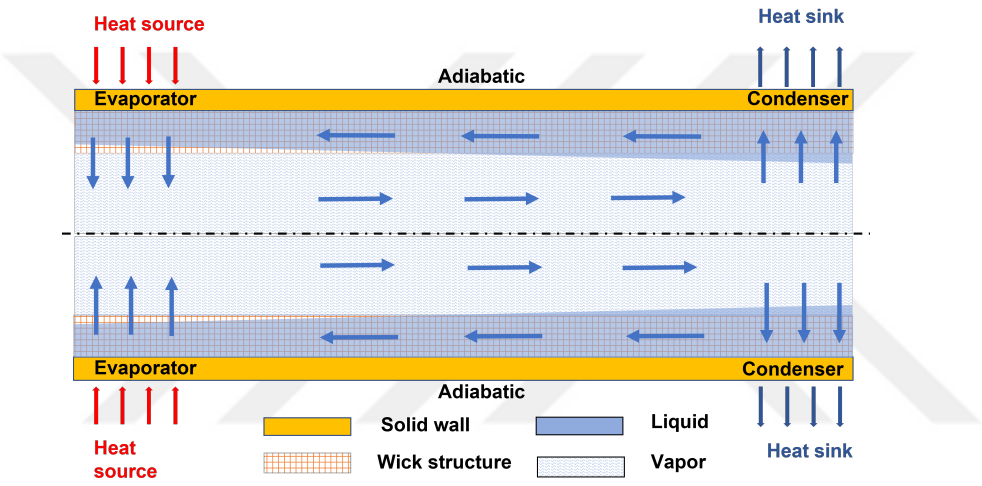

Figure 1.1: Heat pipe working mechanism

Heat is added from an external source which is called the evaporator section, and liquid evaporates and results in vapor flow. Then, the vapor comes to the region, the condenser section, where the temperature is relatively low and turns back to the liquid phase. The mechanism that drives the liquid flow through the evaporator section is the variation of the interface between the vapor and liquid phases. This creates a difference in capillary pressure generated by the wick structure. As there is a temperature difference, flow circulation continues under certain limitations. The capillary structure, wick, has 3 common types which are groove, mesh, and sintered as shown in Figure 1.2.

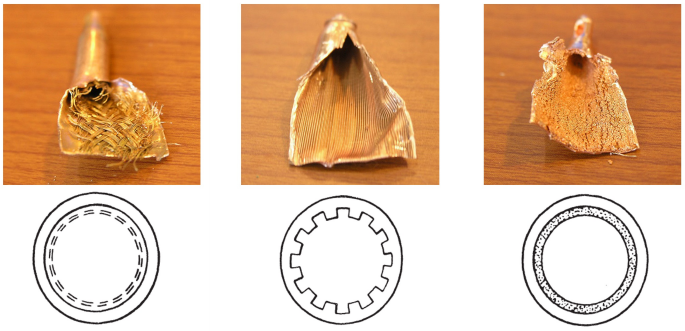

(a) (b) (c)

Figure 1.2: Different wick types (a) mesh (b) groove (c) sinter [6]

According to the application purpose, these types can be hybridized to benefit the advantages in certain points [7,8]. The advantages and disadvantages are summarized in Table 1.1.

Table 1.1: Advantages and disadvantages of wick types

Wick types	**Advantages**	**Disadvantages**
Screen mesh	Manufacturing is easier than sintered wick Lower frictional pressure drop	Average capillary pumping pressure Manufacturing is costly
Groove mesh	Easiest manufacturing Simple structure lends itself to theoretical/numerical modeling	Lowest thermal performance Not operating against gravity
Sintered mesh	Higher capillary pumping pressure due to porous media Ability to operate against gravity	High frictional losses due to small pores lead to dry-out

1.1 Heat Pipe Classification

HPs are classified based on the geometry, capillary structure, and transportation mechanism of liquid. The effects of these variations show themselves in their application areas. In this section 4 different types are summarized.

1.1.1 Conventional Capillary Driven Heat Pipes

Conventional capillary-driven heat pipes are the most common HP in the industry, and they can be cylindrical or flat. The only difference between them is their cross-sections. The capillary structure is determined based on the specifications presented in Table 1.1. Flat heat pipes have an advantage in the thermal management of electronics since they can be placed on the device easily owing to their shapes and they are able to prevent hot spots formation along the plate.

1.1.2 Pulsating Heat Pipes

Pulsating heat pipes which consisted of a tube, compensation chamber and vapor removal channel, are invented in 1995 [9]. There are slugs in the tube formed due to surface tension as shown in Fig.1.3. When the temperature increases at the evaporator, vapor pressure also increases, and it pushes the liquid-vapor mixture to the condenser. Due to the rise in liquid pressure in the condenser, the mixture is propelled toward the evaporator section, where heat is transferred between the two ends of the heat pipe in this process.

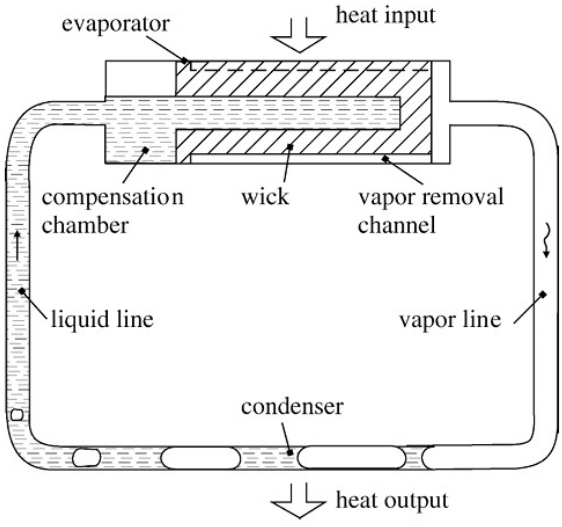

Figure 1.3: Schematic of pulsating heat pipes [10]

1.1.3 Loop Heat Pipes

The distinctive characteristic is that there is a vapor passage apart from the wick structure. LHPs are commonly utilized in space applications due to their ability to function effectively in adverse gravity environments. Also, this type of heat pipe can transmit heat over long distances.

1.1.4 Micro Heat Pipes

Micro heat pipes (MHP) consist of one channel, enclosing vapor, and liquid flow. The main advantage of this heat pipe type is ensuring homogeneous temperature distribution along the heat pipe. In the first studies equivalent diameter is around $1\ \mathrm{mm}$; however, recently this value decreased down to 30 micrometers with the invention of the etching technology. With these advances, narrow channels can be manufactured in the silicon wafer base. Also, cross-section types of the micro heat pipe are given in Fig.1.4. These cross-sections behave as liquid arteries and enhance the capillary structure. MHPs are mostly used in electronic cooling.

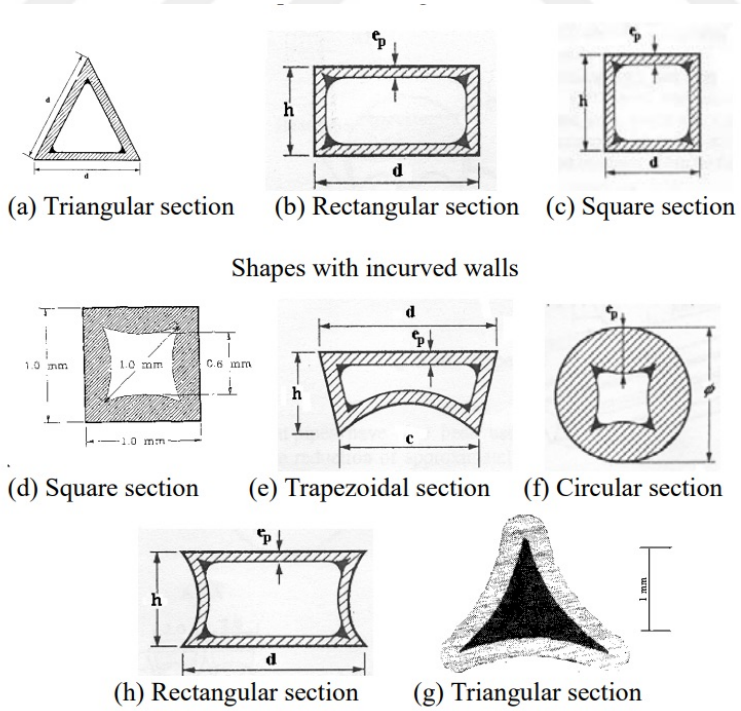

Figure 1.4: Different cross-sections of MHPs [11]

1.2 Definitions

In this section, related physical definitions are explained.

1.2.1 Surface Tension

Surface tension is formed by a lack of cohesive forces at the interface between different substances [12]. This absence induces increased interfacial energy of the materials when the cohesive forces are stronger than adhesive forces.

The contact angle, an indicator of surface tension, is the angle formed between three substances which are the interface between liquid and vapor, and the solid. Fluids can be classified as wetting or non-wetting depending on whether adhesive or cohesive force is dominant. The former type has larger adhesive forces than cohesive forces and its contact angle is lower than 90°. As a result of the unbalance between these forces, the pressure difference at the interface between two fluids is formed, and it is named capillary pressure. The Young-Laplace equation, given in Eq. 1.1, represents capillary pressure with surface tension and radii of interface curvatures.

$$p_c = p_v - p_l = \sigma \left(\frac{1}{R_1} + \frac{1}{R_2} \right) \tag{1.1}$$

where p_c, p_v, p_l, σ, R_1, R_2 represent the capillary pressure, vapor pressure, liquid pressure surface tension, and radius of curvature in the principal directions, respectively. One of the radii of curvature can be considered flat and its radius is relatively too large; therefore, the second term can be neglected becoming Eq. 1.2.

$$p_c = \frac{\sigma}{R} \tag{1.2}$$

Surface tension is a material property that is a function of temperature. It decreases as the fluid temperature decreases. Variations in these conditions create a surface tension gradient resulting in the formation of Marangoni forces. Marangoni forces are examined extensively in many kinds of research and books. These forces become dominant if they are comparable with the gravitational forces. If not such as for macro-scaled systems, they are neglected.

1.2.2 Dry-out

Dry-out is a phenomenon when there is a lack of liquid present in the evaporator section of HP. This may be caused by several factors, including exceeding the maximum heat-carrying capacity (which is discussed in more detail later on) or boiling at the evaporator. Also, the contact angle at the evaporator should not be lower than the material contact angle (α_{ca}) which is the minimum wetting angle of the fluid on the smooth solid surface. In the simulation section of this study, the dry-out occurrence is mentioned when the results can only be obtained by lowering the contact angle at the beginning of the evaporator (θ_{beg},) below the α_{ca}, which is not possible physically.

1.2.3 Working Fluid Selection

Thermofluidic properties of the working fluids determine the transport capacity of HP. High surface tension is required to increase the capillary pumping pressure, while high liquid density and latent heat of vaporization are required to reduce the mass flow rate. Also, low viscosity is desirable to minimize the frictional pressure losses [13]. Merit number is developed to select the proper working fluid and its definition is given in Eq. 1.3.

$$M = \frac{\rho \sigma h_{fg}}{\mu} \tag{1.3}$$

where ρ, σ, h_{fg}, μ are density, surface tension, latent heat of vaporization and dynamic viscosity of the fluid. The Merit number depends on temperature, with a higher number indicating greater transport capacity. The selection of a proper working fluid should also take into account its compatibility with the capillary structure material. Ultimately, the decision on the working fluid should be based on the operating temperature, Merit number, and compatibility with the wick material.

1.2.4 Filling Ratio

Thermal performance highly depends on the amount of working fluid inside the heat pipe. In literature, it is nondimensionalized in order to generalize the quantity, it is

denoted by the filling ratio (FR). In this study, the filling ratio is defined as the ratio between the total volume of working fluid occupied as a liquid and the total groove volume. The mathematical definition is given in the Eq. 1.4.

$$\psi = \frac{V_\ell}{V_g} \tag{1.4}$$

1.2.5 HP Performance Indicators

Heat pipe performance can be evaluated in terms of thermal and hydrodynamic performances. The evaluation indicators are defined as:

- q_{ratio} refers to the ratio of heat transfer with phase change to total heat load (see Eq. 1.5). It indicates the amount of heat that is extracted through the phase change.

$$q_{ratio} = \frac{q_{pc}}{q_{in}} \tag{1.5}$$

- Wall temperature difference (ΔT_{wall}) is the temperature difference between two ends of the HP which is shown with Eq. 1.6. It also gives information about conduction heat transfer.

$$\Delta T_{wall} = (T_{wall})_{max} - (T_{wall})_{min} \tag{1.6}$$

- Q_{max} is the maximum heat that HP can carry without any dry-out formation. This parameter is highly related to the capillary pumping performance of the HP.
- k_{eff} is the effective thermal conductivity of heat pipe. This parameter enables to compare the performance of HP with the other thermal management devices. Eq. 1.7 gives the definition of k_{eff}.

$$k_{\mathit{eff}} = \frac{Q_{in} L_{\mathit{eff}}}{(T_{wall,e} - T_{wall,c}) A_{\mathit{eff}}} \tag{1.7}$$

where Q_{in}, L_{eff}, A_{eff}, $T_{wall,e}$ and $T_{wall,c}$ are total input heat, the effective length of HP, the effective cross-sectional area of HP, wall temperatures at evaporator and condenser, respectively.

- ϵ_{hp} is the effectiveness of the heat pipe which is introduced by Alijani *et al.* [14]. When ϵ_{hp} equals 1, it means that there is no phase change in the heat pipe which refers to low thermal performance. ϵ_{hp} is defined in Eq. 1.8.

$$\epsilon_{hp} = \frac{(\Delta T_{wall})_{dry}}{(\Delta T_{wall})_{operating}} \tag{1.8}$$

In this study, q_{ratio}, Q_{max} and ΔT_{wall} are used to assess the thermal performance of FGHP.

1.3 Literature Review

The thermal performance of heat pipes is an essential criterion to be assessed for the heat pipe design. Therefore, researchers study the thermal performance both numerically and experimentally over the years to assess the heat transfer capacity of heat pipes. To predict the heat pipe performance both fluid flow and thermal analysis should be performed. Energy, momentum, and mass conservation equations and the Young-Laplace law should be solved simultaneously which are nonlinear equations. Therefore, several models with different assumptions are suggested by researchers and presented in Section 1.3.1. Section 1.3.2 is devoted to experimental studies for heat pipes with different groove geometries, base materials, and types.

1.3.1 Numerical studies

After the discovery of the heat pipe, it became an interest for the researchers to understand and improve its concept. Analysis of heat pipe physics requires a coupled solution of fluid flow and thermal analysis. The hydrodynamic model speculates the capillary performance of the wick structure and determines the free-surface geometry, while the thermal model predicts the temperature distribution along the heat pipe and provides an evaluation of the thermal performance. In this study, the models developed for flat grooved heat pipes (FGHP), micro heat pipes (MHP), and vapor chambers (VC) in the literature are reviewed..

The mathematical model developed by Cotter *et al.* [15] predicts the capillary limit to

obtain the maximum heat-carrying capacity of MHP. Incompressible, steady momentum equation for vapor and liquid flow was solved, assuming both flows are laminar and one-dimensional. In order to simplify the solution process, it was assumed that the velocity at the interface and conduction along MHP are zero. In 1990, Babin *et al.* [16] also developed a model with similar assumptions. In addition to their numerical study, they conducted experiments on the triangular grooved MHP and compared the model results with experimental data [16]. It was seen that model and experimental results are not consistent for dry-out occurrence.

In 2005, Jiao *et al.* [17] developed a model to observe the thin film's effect on evaporation and condensation mechanisms. The model was based on the conservation of mass, momentum and energy, and Young Laplace equations. They concluded that contact angle not only specifies the capillary pumping performance but also affects the thin film geometry and the radius of curvature becomes smaller, as the length of the thin film increases. Axial conduction along the wall was neglected similar to [15], [16]. This assumption was validated in 2003 [18] obtaining 1°C wall temperature difference in their MHP. However, the experimental study performed by Hopkins *et al.* [19] showed that this assumption becomes invalid for their MHP configuration which was tested under 100 W. It resulted in over-prediction of the thermal performance of HP. They obtained a 25°C temperature difference at the solid wall which proves the importance of the conduction heat transfer.

Heat pipes consist of liquid and gas flows that are counter-current to each other. As the heat pipes are becoming thinner, the effect of the interfacial interactions and gas flow becomes important to specify the capillary limits and performance of the FGHP, MHP, and VCs. In fact, vapor flow can pull the liquid when the shear stress at the interface is high for some cases. In the literature, some of the studies only focused on the single-phase, liquid flow, assuming constant vapor pressure and temperature along the heat pipe [20–22] while some of the studies include both two-phase flows [23–31].

Ayyaswamy *et al.* [21] modeled the 2D liquid flow in triangular grooves defining the contact angle variation as input and vapor flow was neglected. Galerkin Boundary Method was used to obtain the liquid velocity. The effect of the groove angle and contact angle were investigated. It was discovered that as the contact angle increases,

there is a corresponding increase in pressure loss. In 2005, Suman [22] developed a model and tested it on rectangular and triangular grooved MHP. They investigated the capillary limits of MHP under different inclination angles. They stated that the body force effect creates negligible difference at the interface compared to the capillary pressure on their configurations. They also performed a parametrical study for the capex angle of triangular grooves, finding that increasing the capex angle leads to a decrease in capillary pumping pressure. This model was validated with experimental study [32].

Also, Lefévre *et al.* [33] developed a 2D hydrodynamic and 3D thermal coupled model for MHP with porous capillary structure. The hydrodynamic model is based on both liquid and vapor flows. Vapor flow was modeled as flow between two parallel plates and interfacial shear stress was neglected. The numerical model was validated with the experimental data. In this study, the importance of including pressure drop along the vapor flow was underlined. It was also found that neglecting interfacial shear stress is a valid assumption for relatively lower velocities; however, it becomes significant when the velocities are increased.

There are several studies in the literature that accounts the interfacial shear stress effects studied on the MHPs [28–31, 34, 35]. In 1994, Ma *et al.* [28] introduced a non-dimensional interface flow number which was expressed in terms of vapor, liquid velocities, and dynamic viscosities, to comprehend the interfacial interaction effects. Velocity at the interface was assumed constant along the heat pipe and the experimental data [21] was used to correct the 1D velocity assumption at the interface. This model requires experimental data; therefore, they developed a mathematical model for triangular groove as a further step of the previous study [35]. To be able to solve the vapor and liquid flow which are dependent on each other in terms of the boundary condition at the interface, Nachtsheim-Swigert iteration method and coordinate transformation were used. Furthermore, Khrustalev *et al.* [34] developed a mathematical model and validated their model with the experimental study [36]. They concluded that including shear stress at the free surface highly affects the maximum heat-carrying capacity of MHPs and increases the liquid blocking zone at the condenser. In 2017, Jung et al. [29] conducted a study to analyze how disjoining pressure affects the thermal performance of MHP, they also included the interfacial shear stress

in their models. They found that including disjoining pressure results in obtaining a thinner film region in the liquid phase and affects the phase change heat transfer. One shortcoming of the model is that temperature variation along the solid wall should be assumed priory which was overcome in their further study [37]. In this study, conservation equations applied to both phases were adapted to the thin film geometry and they developed their thermal model by investigating on the thin film. They validated their models with experimental work reaching a maximum of 22% error in the overall thermal resistance of MHP.

According to [38], in 1968, DiCola provided an analytical solution to the conservation of momentum equation for liquid flow assuming uniform interfacial shear stress along the heat pipe, which is not accessible in the literature today. Later, Schneider *et al.* [24] combined the solutions for liquid flow with and without the interaction with vapor flow over rectangular grooves and modeled the vapor flow as being unaffected by the liquid flow and having a zero velocity at the interface. The shear stress between wall and vapor was assumed as equal to the shear stress between liquid and vapor. In addition to this, they developed an expression for the liquid friction factor that accounts for interfacial effects. [25–27, 39] built their hydrodynamic models with this approach. Shah and London correlation [40] was used for the calculation of pressure drop for vapor flow.

Faghri *et al.* [27] developed a 2D model using the finite element method solving both laminar vapor and liquid flows on axial rectangular grooved heat pipes. The shear stress at the liquid and vapor interface was included and vapor velocity was assumed zero at the interface as a boundary condition. The obtained friction factor expression from [24] was used for liquid flow. It was remarked that shear stress at the interface between liquid and vapor is not uniform along the curvature and assuming the interface geometry as flat brings along enormous errors; therefore, interface interaction should be modeled in detail. Neglecting the shear stress at the interface brings about over-prediction of the maximum heat transfer capacity. It was also stated that the shear stress at the interface increases getting closer to the fin. Thomas *et al.* [38] also made a similar assumption on interfacial velocity for trapezoidal grooved HPs. In addition to this, the interfacial shear stress was modeled as constant along the meniscus region. They concluded that interfacial shear is highly effective for larger vapor

velocities, and it limits the maximum carrying heat capacity of HPs. In this study, it was also remarked that if the interfacial stress becomes dominant reversed flow in the liquid domain can be observed for counter-current flow.

In 2019, Patel *et al.* [41] conducted a numerical and experimental study on a cylindrical aluminum HP with a trapezoidal groove and ammonia was selected as a working fluid. In their numerical models, interfacial shear stress was also included. They also performed a parametric study to find the optimum design of groove geometry in which based on maximum heat-carrying capacity, Q_{max}, and minimum overall thermal resistance, R_{tot}, values. It was found that a higher number of grooves enhances the objective parameters until the frictional pressure drop becomes dominant over the capillary pumping pressure.

The model developed by Zimmerman *et al.* [42] differs from other studies since they accounted for the effect of the normal velocity component arising from phase change mass transfer. They developed an expression for pressure drop in the vapor domain due to perpendicular velocity to the main flow and assumed that the vapor is saturated to obtain temperature distribution. According to the performed simulations results on sintered wick heat pipe, vapor flow highly affects the thermal performance at lower vapor temperatures and narrower vapor spacing.

In 2021, Saygan *et al.* [20] developed a model to assess the thermal performance evaluation of heat pipes. It was assumed that vapor pressure and temperature are constant along the heat pipe. Moreover, shear stress at the interface between liquid and vapor was neglected. One-dimensional thermal resistance is constructed including the heat transfer in solid and liquid and heat transfer with phase change. The experiments were conducted in order to validate the model in terms of the wall temperature. Based on the experimental data, the model can predict thermal behavior with good accuracy. The model is suitable to be simulated for both sintered wick and groove wick.

Researchers conducted experimental and numerical studies to analyze how the vapor space impacts the performance of heat pipes. Firstly, both transient and steady model was developed for flat HPs by Vaddakan *et al.* [43] using the finite difference method. They performed a parametric study for vapor space on the flat heat pipe in which the base and wick materials are copper and the working fluid is water. It was

stated that at the same heat load, $10\mathrm{W}$, the phase change mass flow rate and liquid pressure drop increase with the decreased vapor core from $0.8\ \mathrm{mm}$ to $0.4\ \mathrm{mm}$. As a result, decreasing the vapor space results in a larger temperature difference between the condenser and evaporator sections of the heat pipe. However, in 2011, according to the results of the experimental and numerical study of Lips *et al.* [39], overall thermal resistance decreases with reduced vapor space values when the filling ratio is greater than its optimal value. Since it causes the liquid to be trapped in the sides and corners of the FGHP. However, it was observed that the capillary limit was reduced as the vapor spacing was decreased. Furthermore, a critical vapor spacing value was found for liquid confinement formation at the condenser section based on developed the theoretical model for non-working conditions. They concluded that the filling ratio and vapor spacing must be adapted to reach a better performance of FGHP. In addition to that, Huang *et al.* [44] conducted experiments on the vapor chambers with $0.4, 0.6, 0.8, 1.0$ and $1.2\ \mathrm{mm}$ vapor spacing values operating at $10\mathrm{W}$–$240\mathrm{W}$ heat loads and working fluid and wick are water, copper multi-layer mesh, respectively. It was stated that as the vapor space becomes thinner thermal resistance increases due to the increasing restriction to the vapor flow, and it is important to specify the minimum vapor space to obtain optimal thermal resistance.

Another vapor space study was done by Ranjan *et al.* [45] on the ultra-thin vapor chamber by keeping the total thickness of the wick and vapor core constant. Therefore, varying the vapor space thickness affected the capillary geometry and pumping pressure capability. According to obtained experimental results, the vapor space thickness effect has a significant role at higher heat loads and thermal resistance becomes smaller at high heat loads and thinner vapor space. Also, as the vapor core becomes thinner, pressure drop also increases and this limits the capillary pumping capacity. Therefore, the optimization study was done by Weibal *et al.* [46] aiming to reach better performance for vapor chambers by differing the working fluid, heat load and wick characteristics such as porosity, particle diameter etc. In 2018, Yao *et al.* [7] proposed a wick structure hybridizing the tree-shaped groove and screen mesh wick to improve the thermal performance of the vapor chamber. The tested vapor chamber consists of evaporator and condenser plates placed parallel to each other. Also, different cavity heights at the same filling ratio were experimented with while working

against gravity and they found that thermal resistance decreases with increased vapor spacing values, it was explained that flow distance becomes shorter and the required capillary pumping pressure to flow back to the evaporator section becomes smaller. In 2021, Li *et al.* [47] conducted experiments on ultra-thin vapor chambers (UTHV) for different vapor duct thicknesses and different filing ratios. Researchers conducted these experiments on the unprecedented copper UTHV which is designed so that the top plate of the vapor chamber is unwicked and finned and this fin-groove geometry provides improvements both in structural integrity and condensation. This novelty not only provides better anti-dry-out performance but also offers thinner UTHV. Also, the effect of vapor duct thickness on capillary blocking was investigated. It was found that the way to overcome with capillary blocking is by decreasing the amount of the working fluid from the heat pipe. The other outcome is that in the absence of capillary blocking, total thermal resistances of the vapor chamber (R_{vc}) does not show variation for different vapor spacing.

The schematic of the control volume is given in Fig. 1.5. Also, the terms of conversation of momentum on control volume are given in the below equation for the liquid domain.

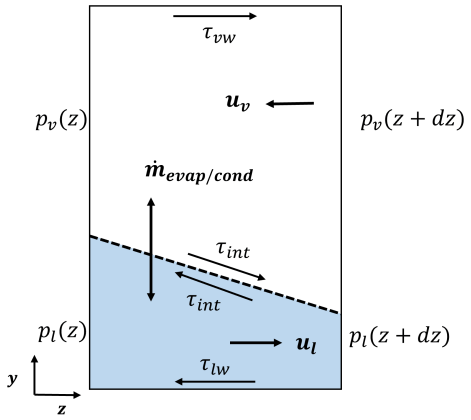

Figure 1.5: Control volume

$$\underbrace{\rho_\ell \frac{d(A_\ell u_\ell^2)}{dz} dz}_{\text{(1) Rate of ch. of mom. in spatial}} = \underbrace{-A_\ell \frac{dp_\ell}{dz} dz}_{\text{(2) Liq. pressure force}} - \underbrace{p_\ell \frac{dA_\ell}{dz} dz}_{\text{(3) Liq. pressure force}} + \underbrace{p_v \frac{dA_\ell}{dz} dz}_{\text{(4) Vap. pressure force}} - \underbrace{\rho_\ell A_\ell g \sin\beta dz}_{\text{(5) Body force}}$$
$$+ \underbrace{\tau_{\ell w} L_{\ell w} dz}_{\text{(6) Wall-liq. shear}} + \underbrace{\tau_{int} L_{int} dz}_{\text{(7) Liq.-vapor shear}} + \underbrace{\frac{dm_{evap}}{dz}(u_{int} - u_\ell) dz}_{\text{(8)Momentum transfer due to phase change}}$$

Table 1.2 shows some studies in which terms are included in their models. These studies include the related terms according to the methodology in different ways.

Table 1.2: Summary of some studies accounting for the terms in the momentum balance of the liquid control volume (Adapted from [23])

Studies	(1)	(2)	(3)	(4)	(5)	(6)	(7)	(8)
Longtin *et al.* [48]	✓	✓	-	-	-	✓	✓*	-
Khrustalev *et al.* [26]	✓	✓		-	-	✓	✓*	-
Ivanova *et al.* [49]	✓	✓	✓	-	-	✓	✓*	-
Schneider *et al.* [24]	-	✓	✓	-	-	✓	✓*	-
Suman *et al.* [22]	-	✓	-	-	-	✓	-	-
Lefevre *et al.* [50]	✓	✓	✓	✓	-	✓	✓*	-
Saygan *et al.* [20]	-	✓	-	✓	-	✓	-	✓

*Vapor is assumed motionless at the interface

1.3.2 Experimental studies

In the literature, different base materials such as silicon, copper, ceramics, and aluminum were experimented in order to validate the numerical models and test the working physics and limitations of HPs. Most of the studies focused on the steady-state performance of HPs under different working conditions and the effects of geometrical parameters.

Firstly, Peterson *et al.* [51] experimented the silicon heat pipes with rectangular and triangular-shaped grooves and found that there are 31% and 81% improvements in effective thermal conductivity comparing the bare silicon plate, relatively rectangular and triangular grooves. They related the better performance of triangular-shaped groove HP with higher capillary pumping pressure due to shaper corners leading to expansion of the meniscus region. In 1999, Hopkins *et al.* [19] investigated the maximum heat-carrying capacity of copper-water heat pipes with trapezoidal and rectangular grooved between $60°$C–$95°$C operating temperatures within intervals. It was

found that capillary is the most limiting parameter in terms of maximum heat transfer capacity. Experimental data shows that heat transfer capacity increases with increasing operating temperatures.

In 2002, Anand *et al.* [32] found that as the tilt angle of a silicon V-shaped FGHP increased, the dry-out region expanded, negatively impacting performance. In 2003, Gillot *et al.* [52] performed experiments on brass and silicon flat axially grooved heat pipes to test the operability of a heat spreader. In order to increase the thermal performance of the thermal spreader, the silicon heat pipe is experimented with since manufacturing narrower grooves is possible. However, the silicon HP with a thickness of $200\mu m$ was damaged during the vacuuming process.

In 2011, the static contact angles between the copper surface and droplets of methanol, water, and acetone were measured by Wong *et al.* [53] within different elapsed times. The measured angle also increases linearly with time; however, acetone and methanol still adhere along the copper surface. They also investigated the evaporation thermal resistance of these working fluids experimentally on the copper mesh wicked FGHP, observing a little difference between the fluids. Also, the study stated that the transition to nucleate boiling is easier for acetone and methanol than water.

Alijani *et al.* [54] conducted experiments on aluminum FGHPs in which different groove densities were manufactured and FGHP effectiveness was evaluated at varying heat loads and filling ratio. It was found that HP performance is highly dependent on groove geometry, heat input, filling ratio, and working fluid. Therefore, these parameters should be selected according to the design requirements.

Apart from focusing on the steady state behavior of HP, the transient analysis is also studied in the literature [55–57]. In 2023, Garimella et al. [57] studied the recovery behavior of HP after dry-out. They obtained the maximum hysteresis line showing the thermal resistance of HP for varying heat input. They constructed their models for dry-out, no dry-out and partial dry-out cases. The numerical model was validated with an experimental study. According to the study, after exceeding the capillary limit of HP, even the heat input reduced thermal resistance cannot be fully recovered up to a certain level of heat loading.

In addition to these experimental studies to understand the working limits of HP, researchers came up with different alternative ideas to improve the thermal performance of heat pipes. Since the driving force of circulation of liquid flow is the capillary pumping pressure, many studies investigated the capillary limits and effects to performance. In the literature mainly 3 main ways were studied to improve the thermal performance of HPs, these are increasing the wettability of solid surface [53, 58–65], using nanofluid as a working fluid [66–71], or modifying the wick geometry to increase the capillary pumping [72–75].

Wettability highly depends on oxidation degree, and roughness of the surface and can be expressed with contact angle between solid and liquid. In the literature generally contact angle range is given for a specific combination of working fluid and solid. Min *et al.* [59] showed the effect of improving the wettability of the copper surface by coating with NaOH and K2S2O8 solutions. They concluded that superior thermal performance is observed compared with the bare version. In 2010, Vasiliev *et al.* [58] performed experiments on the cylindrical trapezoidal grooved heat pipe by coating it with ceramic particles on both evaporator and condenser surfaces. They found that coating with porous material improved the evaporation 1.3–1.8 times, while it deteriorated the condensation performance obtaining higher thermal resistances. In 2020, Kueh *et al.* [62] studied the thermal performance improvement of MHPs with coated Carbon Nano Tubes (CNTs) aiming to increase the hydrophilic characteristics at the evaporator and boost the capillary pumping pressure. They reached 2 times better effective thermal conductivity and 61% improvement in evaporation.

Thermophysical properties are essential for heat transfer; therefore, researchers started to study nanofluids as working fluids in HPs by experimenting with different types of them. For instance, Niu *et al.* [67] reached to up 75% improvements in effective thermal resistance by using Si02-Water instead of using DI water. In addition to this, according to the experimental study [68], using graphene nanofluid leads to 48.4% decrement in overall thermal resistance. However, using nanofluids comes with possible challenges which are potential clogging of the nanoparticle particles, and long-term stability and reliability issues [76].

Wick geometry essentially affects the liquid flow; therefore, it has a significant role

in the capillary pumping performance of HP. Considering this, Nagayama *et al.* [72] proposed a converging channel groove geometry which is the groove width decreases linearly from the condenser to the evaporator region. The capillary effect is highly related to the contact angle, if the contact angle at the evaporator is increased by decreasing the width of the groove it is possible that the heat pipe can operate under higher heat loads. However, decrement in the groove width results in the increment of pressure loss from viscous effects, and thermal performance enhancement could not be achieved. The optimum groove geometry mathematically was studied numerically. According to this, 4 different silicon-based flat heat pipes were manufactured to be able to compare the thermal performances of the heat pipes. The total length of the heat pipe is $70\ \mathrm{mm}$ and the groove height is identical for all configurations. From the condenser to the evaporator end groove widths are $0.3\ \mathrm{mm}$ and $0.1\ \mathrm{mm}$ while the other configuration has $0.4\ \mathrm{mm}$ to $0.2\ \mathrm{mm}$. The other configurations have the constant cross-sectional area and groove widths are $0.3\ \mathrm{mm}$ and $0.1\ \mathrm{mm}$, respectively. Heat input was increased until the surface temperature is reached $100°\mathrm{C}$. They found that effective thermal conductivity for optimized converging channel geometry showed the highest performance for all configurations at every heat load.

In 2020, Hamidnia *et al.* [75] performed experiments to test the effects of different micro pillar shapes, patterns and materials machined in rectangular grooves on the thermal performance of the silicon micro heat pipes. Their study shows that these micro pillars increase contact surface area therefore capillary performance and thermal performance of the heat pipe. Also, they noted that micro-pillar with a diamond shape has the highest effective thermal conductivity. It was clarified that increasing corners improve the capillarity.

The innovative groove geometry was introduced by Saygan *et al.* [73], which is the Hierarchical Groove Architecture (HGA). The groove geometry is defined as grooves are straight from the beginning of the condenser up to the evaporator region. From the evaporator point grooves are branched into narrower channels. The main purposes of branching are improving capillary pumping and evaporation enhancement. Experiments were performed on the 3 different copper heat pipes and IPA was used as a working fluid. For all tested heat pipes length of the evaporator, adiabatic and condenser regions, and groove and base heights are kept identical to each other. Two

of the heat pipes have constant groove cross-sections having $0.3\,\mathrm{mm}$ and $0.6\,\mathrm{mm}$ groove widths and the number of grooves is 38 and 19, respectively. In the other heat pipe with HGA, the groove width is $0.6\,\mathrm{mm}$ and decreases to $0.3\,\mathrm{mm}$ at the evaporator region while the number of grooves increases from 19 to 38 at the evaporator. The study states that branching helps to increase capillary pumping and evaporation enhancement. Experimental and numerical results show that heat pipe with HGA gives a large temperature difference along the wall compared with other configurations. This was explained as increasing the contact angle at the evaporator leads to an increase in thermal resistance. However, according to the simulations, this effect can be reduced when the number of branching increases. Since the manufacturing of thinner channels on the copper base is challenging, experiments were ended.

1.4 Objective and Outline of Study

The objective of the study is to develop a comprehensive model to assess the effect of vapor flow that mimics the FGHP to evaluate thermal performance. In addition to the numerical study, experiments are conducted to characterize the effect of vapor flow under various operating conditions, including different heat loads and filling ratios. The findings will contribute to a deeper understanding of vapor flow and interfacial effects, facilitating the design and optimization of these heat transfer devices for enhanced thermal management in a wide range of applications. Also, the effects of the vapor flow on the thermal performance and the physical reasoning behind it are not fully explained in the literature for FGHPs. The outline of the study is as follows.

In Chapter 1, physical definitions and literature review related to the scope of the thesis are introduced which helps to establish a necessary background. In Chapter 2, firstly developed numerical model is explained by dividing into fluid flow model and thermal analysis. Then, the experimental setup and procedure are explained. Chapter 3 includes the validation study of the developed model and simulation results for FGHP with varying vapor space thicknesses. Then, experimental results and observations are given. Finally, Chapter 4 summarizes the work and points out the remarks.

CHAPTER 2

METHODOLOGY

2.1 Numerical Modeling

Modeling FGHP physics needs an analysis of fluid flow and heat transfer which are strongly dependent on each other due to the presence of phase change and a free surface. Therefore, it was studied extensively over the years by various simplifications as mentioned in Chapter 1.

The developed model that neglects the vapor flow is used to evaluate the performance of different configurations of FGHP under various heat loads until dry-out occurs [20]. In this study, the vapor flow solution is constructed within the structure of this methodology by expanding the model. In this section, after explaining the solution procedure of the model, details of the flow model and thermal network are outlined in Sections 2.1.1 and 2.1.2, respectively.

The model needs specifications of geometrical details and operating conditions of FGHP to simulate. Operating conditions are total heat load (q_{in}), coolant temperature (T_c), and coolant heat transfer coefficient (h_{conv}), the geometric parameters are wick geometry (w_g, w_f, h_g), lengths of the adiabatic (L_a), evaporator (L_e), and condenser (L_c) regions, and height of the vapor flow cross-section (h_v).

FGHP is divided into slices to achieve better accuracy. Both flow and thermal models are constructed based on the divided slices. Firstly, phase change heat transfer (q_{pc}) and vapor temperature distributions ($T_v(z)$) are estimated before the solution begins. The fluid flow model starts to solve the conservation of mass, and momentum equations by using these initial guesses. The pressure distribution of liquid ($p_\ell(z)$) and

vapor ($p_v(z)$) are found based on the conservation equations. After that, by using Eq. 1.1 the radius of curvature distribution, $\mathcal{R}(z)$, is calculated as well as the edge angle variation along the heat pipe, $\theta(z)$. It is noteworthy that utilizing the edge angle, rather than the contact angle, is a more appropriate approach from a physical perspective. The reason is that there is no contact line between the three phases (liquid, vapor and solid) due to the liquid film at the fin top of the condenser section. Consequently, a more comprehensive definition, namely edge angle is used for discussing the variation along the HP. However, the terminology of contact angle can be applied to the evaporator section.

Then, the thermal resistance network uses the $\theta(z)$ as input for the calculation of thermal resistances. Thermal analysis is constructed based on the conservation of energy with several assumptions. Also, It models the phase change resistances and conduction in solid and liquid domains for the evaporator, adiabatic and condenser sections. Wall temperature distribution, $T_w(z)$, q_{pc} and $T_v(z)$ are the outcomes of the thermal network. Error is calculated considering the previous step and the iterative solution continues until the convergence criteria is achieved. The flow chart of the solution procedure is presented in Fig. 2.1.

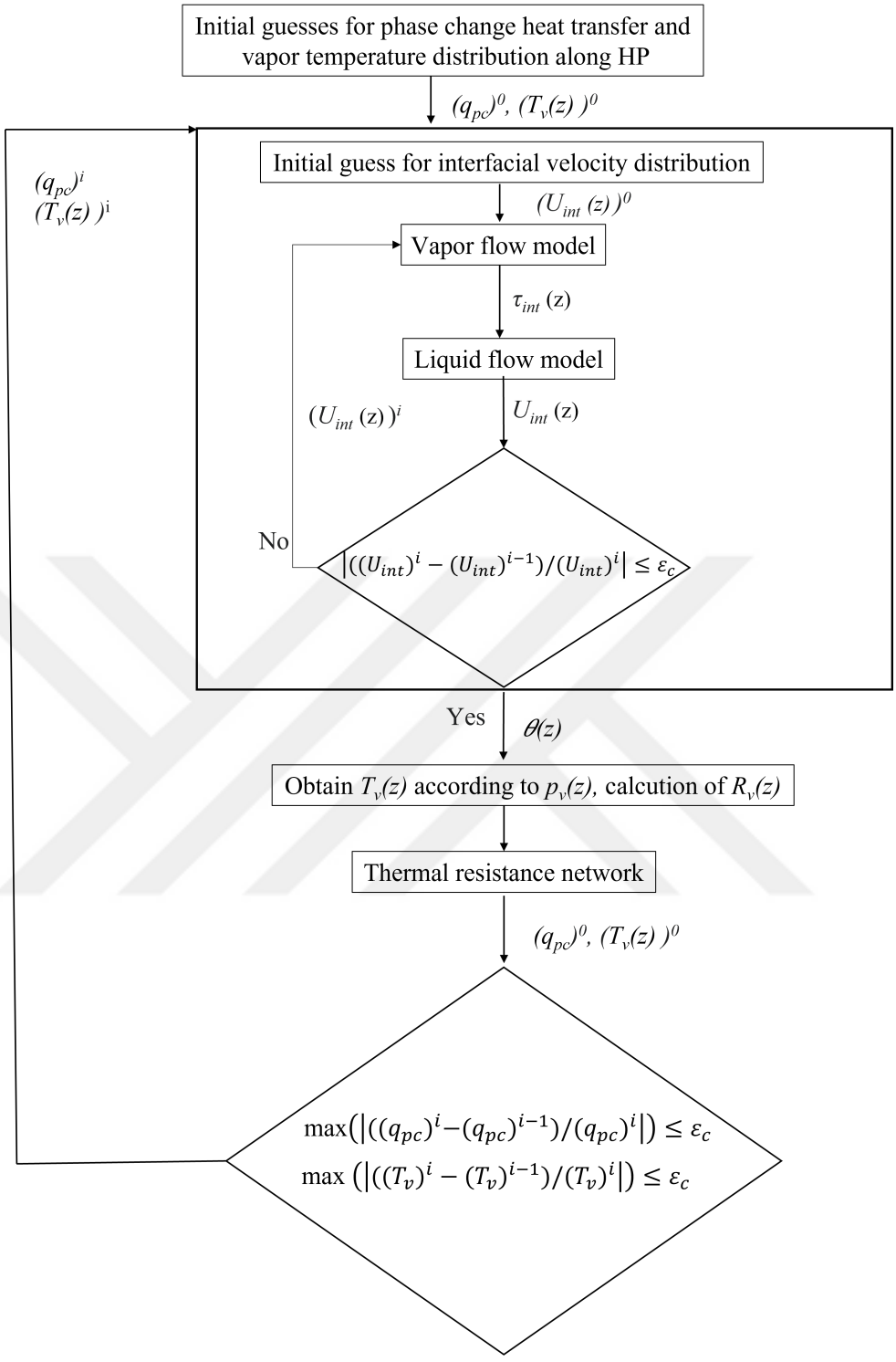

Figure 2.1: Flow chart of the solution procedure

2.1.1 Flow Model

The flow model consists of both vapor and liquid flow analysis including the interactions between the liquid and vapor flows. An iterative process is developed to meet the equality of shear stress (τ_{int}) and velocity (U_{int}) at the interface between liquid and vapor. In addition to the initial q_{pc} and $T_v(z)$ estimations, interfacial velocity distribution, $U_{int}(z)$, is also guessed to start the solution procedure. Initially, vapor flow is solved by taking $U_{int}(z)$ as a boundary condition. Based on the vapor solution, $\tau_{int}(z)$ is calculated and it is used as the boundary condition at the interface for liquid flow. Eq. 2.1 and 2.2 are the governing equations that represent the conservation of mass and momentum respectively, for both liquid and vapor.

$$\nabla \cdot (\rho \mathbf{u}) = 0 \tag{2.1}$$

$$(\mathbf{u} \cdot \nabla)\mathbf{u} = -\frac{1}{\rho}\nabla p + \nu \nabla^2 \mathbf{u} + \mathbf{f_b} \tag{2.2}$$

where ρ, $\mathbf{u}$, p, ν, and $\mathbf{f_b}$ correspond to density, velocity field, pressure, kinematic viscosity, and body acceleration, respectively. Fig. 2.2 represents the physical domains of liquid and vapor.

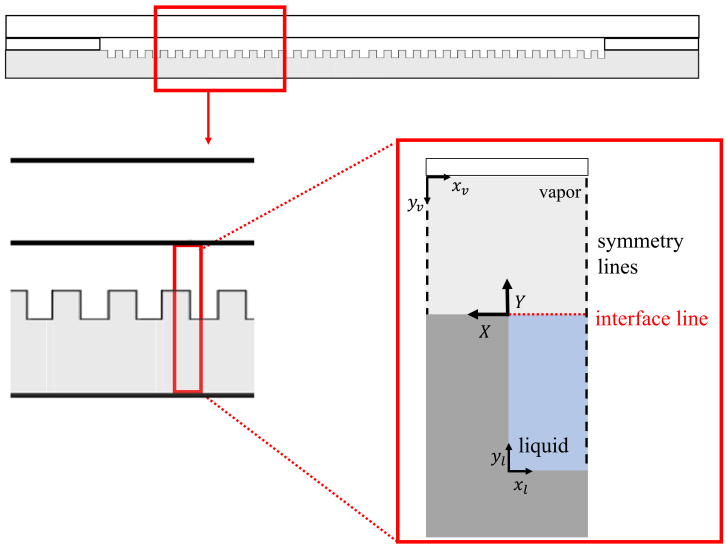

Figure 2.2: Physical domain of vapor and liquid flows

Eq. 2.1 and 2.2 are solved analytically based on the listed assumptions:

- Both liquid and vapor flows are steady, laminar, and incompressible.
- Flow is assumed unidirectional in $z-$ direction.
- Inertial term in Eq. 2.2 is neglected for both flows due to the low mass flow rates.
- Interface geometry between liquid and vapor is assumed to be flat.

Eq. 2.3 describes the conservation of momentum in $z-$ direction after the listed assumptions.

$$\frac{\partial^2 U}{\partial x^2} + \frac{\partial^2 U}{\partial y^2} = \frac{1}{\mu}\frac{dp}{dz} - \frac{1}{\nu} f_z \tag{2.3}$$

where U, p, μ, ρ and f_z correspond to z component of velocity, pressure, dynamic viscosity, density, and body acceleration in the $z-$ direction, respectively, and the equation is valid both for vapor and liquid flows. Also, Eq. 2.4 describes the relationship between mass flow rates of liquid ($\dot{m}_\ell$) and vapor ($\dot{m}_v$) considering the mass transfer by phase change and conservation of mass.

$$\dot{m}_v = -\dot{m}_\ell \tag{2.4}$$

Also, the mass flow rate is calculated based on the q_{pc} estimation for all slices. It is assumed that there is a linear increase in the $\dot{m}_\ell(z)$ in the condenser, and a linear decrease in the evaporator which is the vice versa for $\dot{m}_v(z)$. Also, based on the adiabatic assumption there is no phase change along the adiabatic region, the mass flow rate is assumed to be constant [11, 27, 31, 50, 77–79].

$$\dot{m_{v,\ell}}(z_i) = (E_{v,\ell})_{0,i} z_i + (E_{v,\ell})_{1,i}, \qquad 0 \leq z_i \leq L_e \tag{2.5}$$

$$\dot{m_{v,\ell}}(z_i) = (A_{v,\ell})_{0,i}, \qquad L_e \leq z_i \leq L_e + L_a \tag{2.6}$$

$$\dot{m_{v,\ell}}(z_i) = (C_{v,\ell})_{0,i} z_i + (C_{v,\ell})_{1,i}, \qquad L_e + L_a \leq z_i \leq L_e + L_a + L_c \tag{2.7}$$

After specifying $\dot{m}_\ell(z)$ and $\dot{m}_v(z)$, Eq. 2.3 is solved analytically using separation of variables and superposition for vapor flow. Boundary conditions for both liquid and vapor domains are presented in Fig. 2.3.

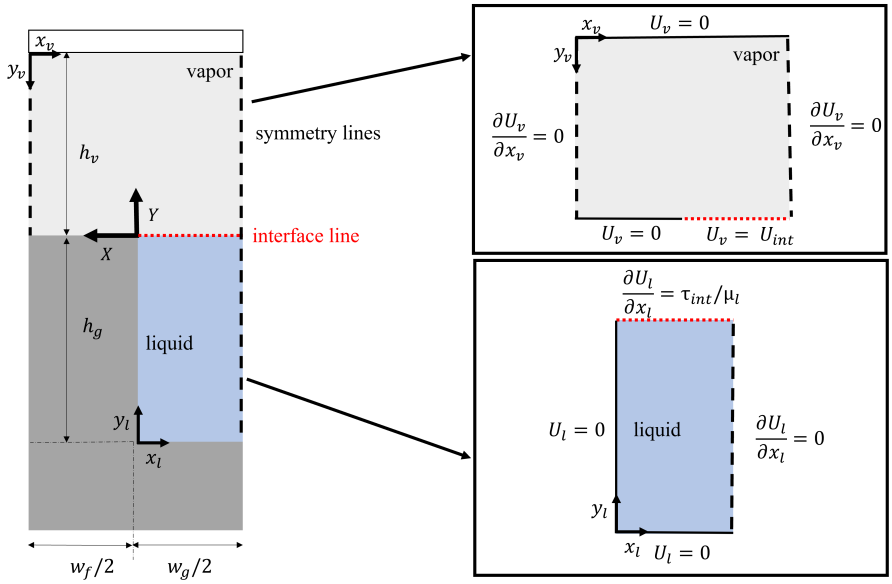

Figure 2.3: Boundary conditions for analytical solution of vapor and liquid domains

Vapor velocity distribution, $U_v(x_v, y_v)$, is given in the Eq. 2.8.

$$\begin{aligned} U_v(x_v, y_v) = & \frac{1}{2\mu}\frac{dp_v}{dz_v}(y_v^2 - h_v y_v) + \frac{w_g}{h_v}\frac{y_v}{w_v} \\ & - 2\sum_{n=1}^{\infty} U_{int}\frac{1}{n\pi}\sin(\lambda_{n,v} w_f)\cos(\lambda_n, vx_v)\frac{\sinh(\lambda_{n,v} y_v)}{\sinh(\lambda_{n,v} h_v)} \end{aligned} \tag{2.8}$$

where $w_v = w_f + w_g$, $\lambda_{n,v} = (2n-1)\pi/(2w_v)$, p_v, μ_v, h_v, w_g, w_f, U_{int} are vapor pressure, dynamic viscosity, vapor space thickness, groove width, fin width and velocity at the interface, respectively. From the definition of mass flow rate which is given in the Eq. 2.9, U_v is integrated over the vapor domain.

$$\dot{m}_v = \int_0^{(w_g+w_f)/2}\int_0^{h_v} \rho_v U_v dx_v dy_v \tag{2.9}$$

It is possible to express $\dot{m}_v(z)$ as Eq. 2.10 combining the Eq. 2.8 and Eq. 2.9.

$$\dot{m}_v(z) = \mathcal{G}_v \left(\frac{dp_v}{dz_v} - \rho_v f_z \right) + \mathcal{H}_v U_{int}(z) \tag{2.10}$$

where $\mathcal{G}_v$ and $\mathcal{H}_v$ are constants of vapor pressure gradient and U_{int}, respectively. $p_v(z)$ can be written as:

$$p_v(z) = \int \left(\frac{\dot{m}_v(z) - \mathcal{H}_v U_{int}(z)}{\mathcal{G}_v} + \rho_v f_z \right) dz \tag{2.11}$$

The equations that describe the pressure distribution in the evaporator, adiabatic, and condenser regions are expressed in Eq. 2.12 by combining Eq. 2.11 and Eq. 2.7.

$$\begin{aligned}
p_v(z) &= \int \left(\frac{E_{v,0} z + E_{v,1} - \mathcal{H}_v U_{int}(z)}{\mathcal{G}_v} + \rho_v f_z \right) dz, \quad 0 \le z \le L_e \\
p_v(z) &= \int \left(\frac{A_{v,0} - \mathcal{H}_v U_{int}(z)}{\mathcal{G}_v} + \rho_v f_z \right) dz, \qquad L_e \le z \le L_e + L_a \\
p_v(z) &= \int \left(\frac{C_{v,0} z + C_{v,1} - \mathcal{H}_v U_{int}(z)}{\mathcal{G}_v} + \rho_v f_z \right) dz, \quad L_e + L_a \le z \le L_e + L_a + L_c
\end{aligned} \tag{2.12}$$

Boundary conditions are needed to obtain the $p_v(z)$. They are given in Eq. 2.13 and 2.14. At the beginning of the evaporator, the pressure value is calculated based on the saturation pressure corresponding estimated vapor temperature.

$$p_v|_{z=0} = T_v|_{z=0} \tag{2.13}$$

$$\left. \frac{dp_v}{dz} \right|_{z=L} = 0 \tag{2.14}$$

Furthermore, the pressure values and their derivatives must be continuous at the transition points between the sections providing the continuity of the pressure distribution, which are given in Eq. 2.15.

$$\int \left(\frac{E_{v,0} z + E_{v,1}) - \mathcal{H}_v U_{int}(z)}{\mathcal{G}_v} + \rho_v f_z \right) dz = \Big|_{z=L_e} \int \left(\frac{A_{v,0} - \mathcal{H}_v U_{int}(z)}{\mathcal{G}_v} + \rho_v f_z \right) dz$$
$$\int \left(\frac{A_{v,0} - \mathcal{H}_v U_{int}(z)}{\mathcal{G}_v} + \rho_v f_z \right) dz = \Big|_{z=L_e+L_a} \int \left(\frac{C_{v,0} z + C_{v,1} - \mathcal{H}_v U_{int}(z)}{\mathcal{G}_v} + \rho_v f_z \right) dz \tag{2.15}$$

After obtaining the $p_v(z)$, every term in Eq. 2.8 is known. Thus, shear stress at the interface, $\tau_{int}(z)$, can be calculated from Eq. 2.16 at the midpoint of the interface where $x_v = w_f + w_g/2$.

$$\tau_{int}(z) = \mu_v \frac{\partial U_v}{\partial y}\Big|_{x_v = w_f + w_g/2} \tag{2.16}$$

Subsequently, $\tau_{int}(z)$ is used as a boundary condition for the liquid flow solution of Eq. 2.3. Similarly, it is solved by using the separation of variables and the superposition. Schematic of the liquid domain with boundary conditions is given in the Fig. 2.3. Liquid velocity distribution, $U_\ell(x_\ell, y_\ell)$, is given in the Eq. 2.17.

$$\begin{aligned} U_\ell(x_\ell, y_\ell) = &\sum_{m=1}^{\infty} \sum_{n=1}^{\infty} \frac{-64}{\mu_\ell} \frac{dp_\ell}{dz_\ell} \frac{(w_g/2)^2 h_g^2 \sin(\lambda_{n,l} x_\ell) \sin(\beta_m y_\ell)}{\pi^4 ((2n-1)^2 h_g^2 + (2m-1)^2 (w_g/2)^2)} \\ &+ \sum_{m=1}^{\infty} \frac{-\tau_{int}}{\mu_\ell} \frac{4 w_g}{(2n-1)^2 \pi^2} \frac{\sin(\lambda_{n,l} x_\ell) \sinh(\lambda_{n,l} y_\ell)}{\cosh(\lambda_{n,l} h_g)} \end{aligned} \tag{2.17}$$

where $\lambda_{n,l} = (2n-1)\pi/w_g$, $\beta_m = (2m-1)\pi/(2h_g)$, p_ℓ, μ_ℓ, h_g, τ_{int} are liquid pressure, the dynamic viscosity of the liquid, groove height and shear stress at the interface, respectively.

Similar operations are repeated to find $\dot{m}_\ell$ and p_ℓ relation in the liquid domain. However, it is written in terms of $\tau_{int}(z)$ instead of $U_{int}(z)$.

$$p_\ell(z) = \int \left(\frac{\dot{m}_\ell - \mathcal{H}_\ell \tau_{int}}{\mathcal{G}_\ell} - \rho_\ell f_z \right) dz \tag{2.18}$$

$$
\begin{aligned}
p_\ell(z) &= \int \Big(\frac{E_{\ell,0} z + E_{\ell,1} - \mathcal{H}_\ell \tau_{int}(z)}{\mathcal{G}_\ell} + \rho_\ell f_z \Big) dz, && 0 \leq z \leq L_e \\
p_\ell(z) &= \int \Big(\frac{A_{\ell,0} - \mathcal{H}_\ell \tau_{int}(z)}{\mathcal{G}_\ell} + \rho_\ell f_z \Big) dz, && L_e \leq z \leq L_e + L_a \\
p_\ell(z) &= \int \Big(\frac{C_{\ell,0} z + C_{\ell,1} - \mathcal{H}_\ell \tau_{int}(z)}{\mathcal{G}_\ell} + \rho_\ell f_z \Big) dz, \\
& && L_e + L_a \leq z \leq L_e + L_a + L_c
\end{aligned}
\tag{2.19}
$$

Boundary conditions need to be defined for the integration given in Eq. 2.18. At the beginning of the evaporator, p_ℓ is calculated from the Young-Laplace equation based on the edge angle, which is given in Eq. 2.20. Also, at the end of the condenser pressure gradient reaches zero as long as there is no pool region, which is given in Eq. 2.21.

$$
p_\ell|_{z=0} = p_v|_{z=0} - \frac{\sigma}{R_{z=0}} \tag{2.20}
$$

$$
\frac{dp_\ell}{dz}\Big|_{z=L} = 0 \tag{2.21}
$$

Then, $U_{int}(z)$ can be recalculated based on the $p_\ell(z)$ obtained from the liquid flow solution. Calculated $U_{int}(z)$ is sent to vapor flow solution and the overall procedure continues until the convergence is reached between the $U_{int}(z)$ results.

After reaching the convergence of the vapor and liquid flow models, $p_\ell(z)$ and $p_v(z)$ are obtained. Moreover, $\theta(z)$ is calculated using the Young-Laplace equation.

2.1.2 Thermal Analysis

Heat transfer is analyzed by the quasi 3D-dimensional thermal resistance network to model the conduction in solid and liquid, and phase change heat transfer along the heat pipe. The obtained $\theta(z)$ from the flow model, is used for calculating the thermal resistances. Phase change heat rates are modeled based on the kinetic theory findings. A similar approach is constructed both for the evaporator and condenser region. There are additional conduction and phase change thermal resistances corresponding to fin top liquid film at the condenser. The film thickness on the fin top is based on 4th order polynomial approach as introduced by Faghri *et al.* [26].

In addition, instead of solving the energy equation along the vapor, it is assumed that vapor is saturated and $T_v(z)$ is found from the corresponding $p_v(z)$ distribution. This assumption is reasonable owing to the low thermal conductivity of vapor. Due to the same reason, conduction in liquid is also neglected only in the axial direction. Besides that, additional computation effort would be required with a little effect on the energy balance compared with the amount of heat transfer with phase change between liquid and vapor, and conduction in the solid.

Based on this assumption, vapor conduction resistances, $R_v(z)$, are added into the network which is calculated with Eq. 2.22.

$$(R_v)_i = \frac{(T_v)_{i+1} - (T_v)_i}{\sum_{n=1}^{i}(q_{pc})_i} \tag{2.22}$$

The energy equation is analyzed by the thermal resistance network given in Fig. 2.4.

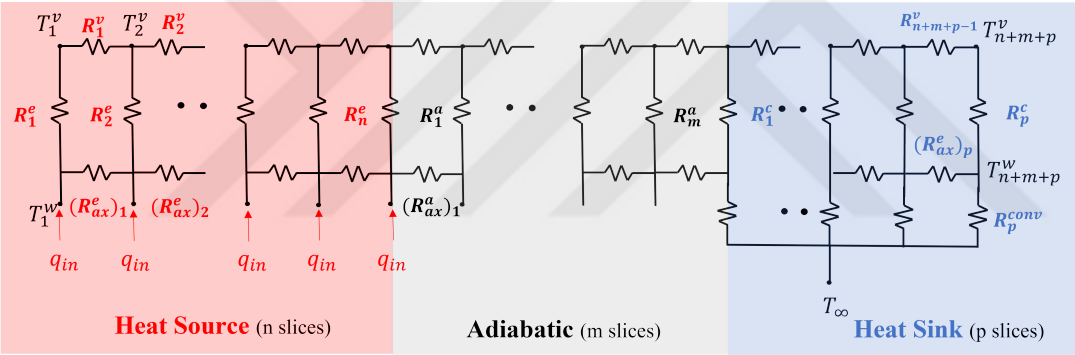

Figure 2.4: Thermal resistance network

Further details about calculations of the resistances are explained in [80], they are modified for varying vapor temperature distributions. Schematic of thermal resistances and circuit representation for the evaporator and condenser sections are summarized in Fig. 2.5.

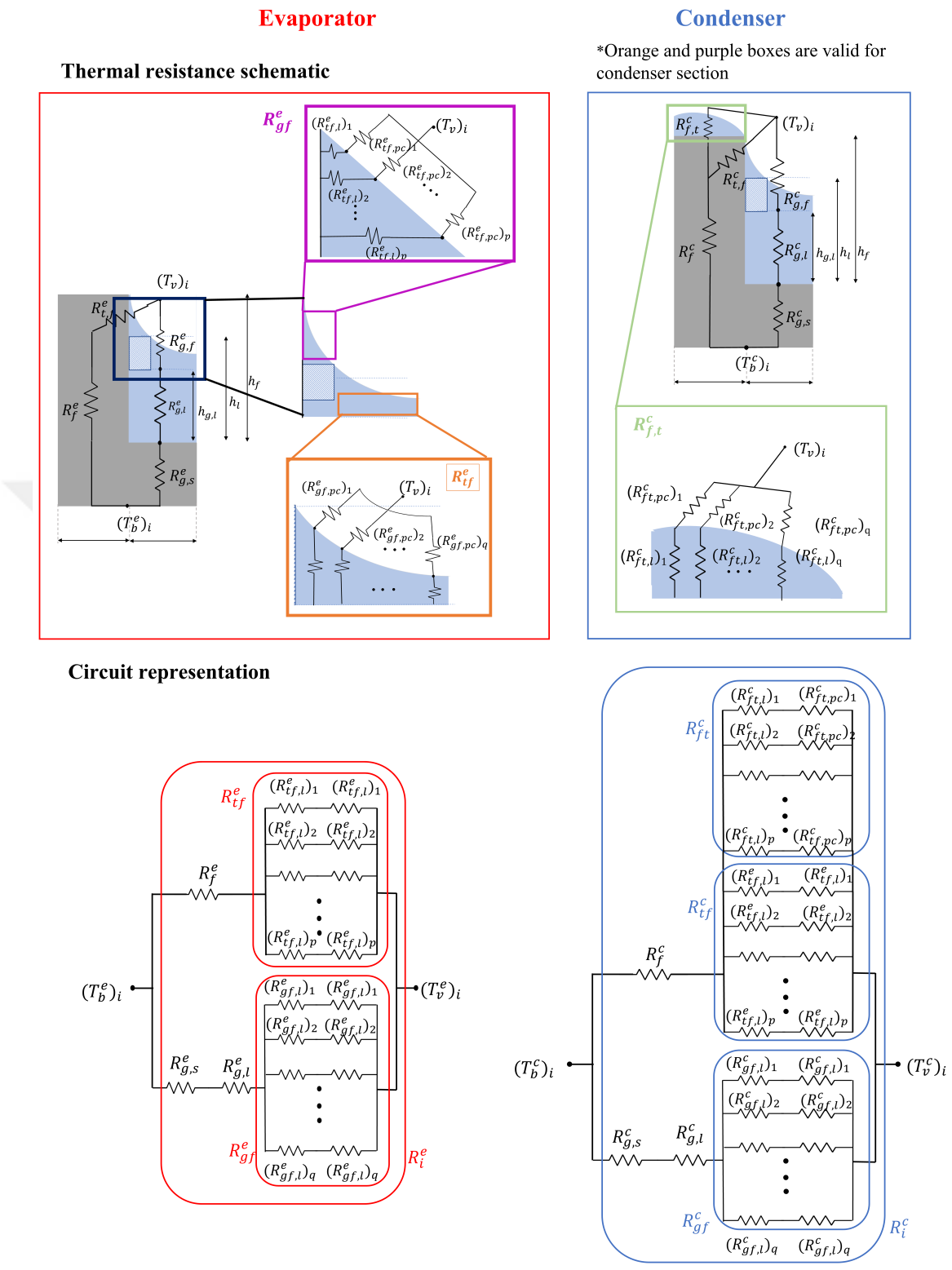

Figure 2.5: Schematic of thermal resistance and circuit representation for evaporator and condenser sections

2.2 Experimental Work

The experimental setup, depicted in Fig. 2.6, was constructed by Saygan [80] in 2021 consisting of the chiller, power unit for heating, vacuum pump, heat pipe assembly and vacuum chambers for solids and working fluid.

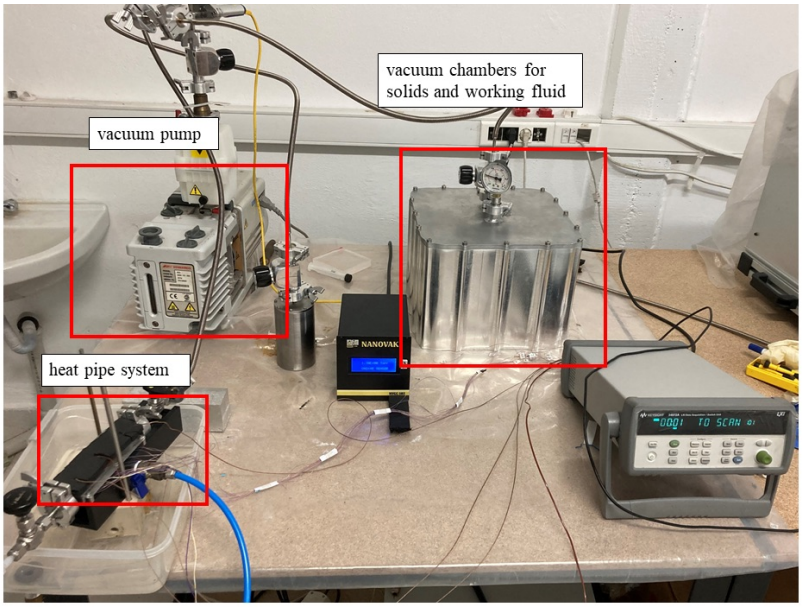

Figure 2.6: Experimental setup

Components of FGHP assembly, top plate, main frame, groove frame, condenser and evaporator, are introduced in Fig. 2.7. The top plate is made of acrylic, which not only allows observation of the operations in the flat grooved heat pipe but also not undergoes chemical reactions with the working fluid under high operating temperatures. This top frame can be altered easily to due to the modular experimental design. The main frame, on the other hand, was constructed of stainless steel, which has low thermal conductivity, aimed at minimizing the conduction in the main frame. The groove frame comprises axial rectangular grooves that form the wick structure of the heat pipe, while thermocouples are positioned beneath this frame to acquire the temperature distribution across the wall.

Lastly, both the evaporator and condenser parts were made of copper due to their high thermal conductivity. The condenser blocks and plate was designed to maintain a constant temperature at the condenser section, with the main objective being to

obtain the minimum thermal resistance. Also, the evaporator is comprised of RF resistors that turn electrical power into heat. The evaporator plate in which resistors are placed was designed based on constant heat flux conditions. Details of the design processes were given in [80]. All of these components are mounted with screws, and thermal paste is used to eliminate contact resistance that may occur at the grooved frame with evaporator and condenser interfaces.

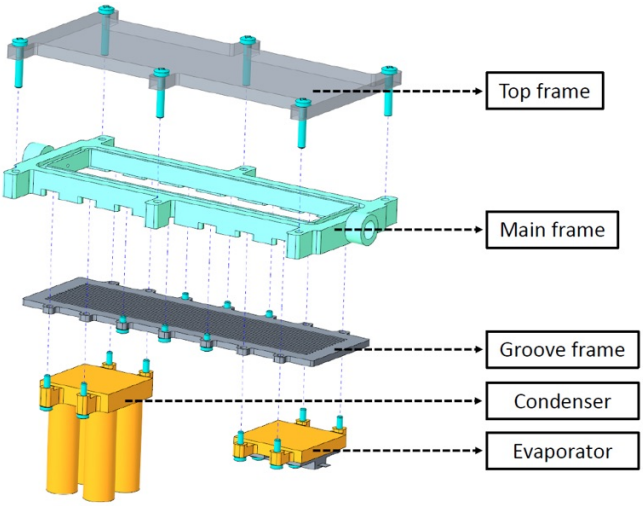

Figure 2.7: Components of FGHP assembly [80]

This experimental setup was tested in terms of operability in a vacuum environment as mentioned in [80]. Therefore, the main framework, in which vacuuming and charging operations are performed, is kept the same. All new components are designed based on the pre-designed component.

Firstly, experimental preparation and procedure are explained in sections 2.2.1 and 2.2.2, respectively. Then, the experimental study is grouped into two which are introduced in sections 2.2.3 and 2.2.4.

2.2.1 Experimental Preparation

A detailed experimental preparation was followed in order to accurately measure and analyze the heat transfer characteristics of the FGHP. Experimental components are placed inside vacuum chambers to avoid outgassing. Outgassing refers to the release of trapped gases within solids and liquids, which can lead to a rise in pressure within

the HP, thereby hindering and deteriorating its performance.

Before starting the experiments, the vacuum condition within the FGHP is tested in order to observe whether there is leakage in the HP assembly. The pressure in the FGHP is measured at the different periods as given in Table 2.1.

Table 2.1: Measured pressures inside the FGHP

Period of time	1st Test	2nd Test	3rd Test	Mean	Standart Deviation
Initial Pressure	1.9 Pa	2.7 Pa	4.0 Pa	2.9 Pa	37.0%
After 12 hours	12.0 Pa	14.7 Pa	8.0 Pa	11.6 Pa	29.1%
After 24 hours	561.3 Pa	623.9 Pa	385.3 Pa	123.7 Pa	23.6%
After 48 hours	1145.2 Pa	1230.6 Pa	978.6 Pa	128.2 Pa	11.5%

The saturation pressure at $30°$C is 8300 Pa. Also, it is observed that pressure rises up to 5 Torr (667 Pa) 24 hours after stopping the vacuum pump which is lower than 10% of the saturation pressure. In addition, each experiment set is completed within 24 hours in order to operate in more convenient vacuum conditions.

2.2.1.1 Thermocouple Calibration

As a preparation, thermocouples are mounted on the tested HP using 2-part epoxy. There are 15 and 3 thermocouples placed on the groove and top frame, respectively. The thermocouple type is T-type and its uncertainty is $\pm 0.5°$C given by the manufacturer datasheet.

Also, calibration is performed before the experimentation. The experimental setup is placed in an insulated environment without having any heat source or sink. Temperature measurements were made in this environment for 16 hours. The mean value of the measured values for all thermocouples is accepted as a reference temperature, T_{ref}. Thermocouples on the wall are calibrated based on the reference temperature.

2.2.2 Experimental Procedure

Before conducting experiments, a vacuum pump is used to remove the air from the HP. Once it is ensured that no air is present in the system, the working fluid is charged into the FGHP assembly which is given in Fig. 2.8. The filling process was described in detail by Saygan [80], and all steps listed below, are followed in this study.

- The syringe is filled with the working fluid that is held in the vacuum environment for outgassing, while valve 2 connected to the syringe is closed. The syringe is connected to the FGHP.
- Valve 2 close to the charging section is opened slowly ensuring that the passage between the syringe and main frame is filled with working fluid instead of air. The valve is closed.
- The valve 1 placed on the other end of HP is opened. The vacuum pump starts to vacuum the FGHP until the pressure drops below 0.04 Torr.
- After reaching the vacuum environment, valve 1 is closed and the heat pipe and all parts for connection are in the vacuum.
- Now the vane 2 is opened and the heat pipe is charged with the working fluid.

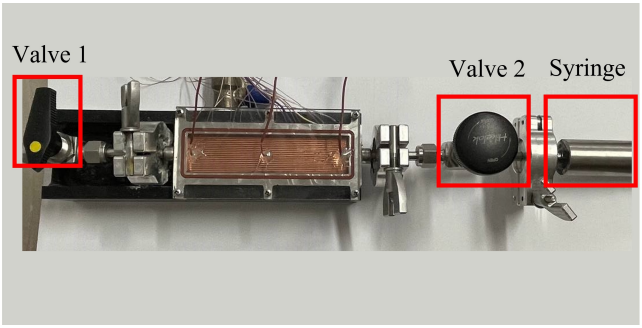

Figure 2.8: HP assembly for charging the working fluid

After charging the system, the chiller is used to set the desired temperature, and cooling water is circulated from the condenser section of the FGHP. Additionally, the power unit is activated for heating at the evaporator. Temperature values are then recorded in the computer via Keysight 34972A data acquisition unit until the system reaches a steady state.

2.2.3 Vapor Flow Experiments

Experiments are carried out to validate the developed model and observe the effects of vapor flow and interfacial effects on thermal performance under various operational conditions. HP can operate within the range $\alpha_{\text{ca}} \leq \theta \leq 90°$. Vapor flow experiments are performed on the copper-IPA FGHP. Since the material contact angle highly depends on the surface quality, it is measured in a laboratory instead of using the value given in the literature. In Fig. 2.9, the photograph of an IPA droplet on the copper surface is given. Using photographs of different IPA droplets, the range is specified as $14° \leq \alpha_{\text{ca}} \leq 27°$ for IPA and copper specimens. The accuracy of the measurement is insufficient due to the limitations of the measurement technique. Nonetheless, it was performed to gain insights into the material contact angle. Based on the measurements, α_{ca} is chosen as $15°$ which is in the measured range.

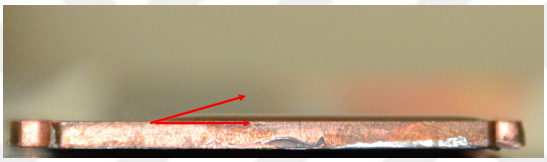

Figure 2.9: Copper-IPA material contact angle measurement

To determine the tested vapor spacing values, different configurations are simulated within the $\alpha_{\text{ca}} \leq \theta \leq 90°$, and the results are tabulated in Table 2.2.

Table 2.2: Simulation results of wall temperature difference range for different vapor space thicknesses at different heat loads

	ΔT [°C]			
Q	$h_v = 2$ mm	$h_v = 3$ mm	$h_v = 4$ mm	$h_v = 6$ mm
9.0 W	–	6.8–9.9	7.1–10.7	7.3–11.3
8.0 W	5.6–6.6	6.3–9.6	6.5–10.3	6.6–10.7
7.0 W	5.1–7.4	5.7–9.1	5.8–9.6	5.9–10
5.5 W	4.5–6.9	4.6–8	4.7–8.4	4.7–8.7
4.0 W	3.4–5.9	3.4–6.6	3.4–6.9	3.4–7.0

The vapor spacing values were selected based on their measurability in terms of temperature differences at the solid wall. According to Table 2.2, $h_v = 4$ mm have similar behavior with $h_v = 6$ mm. Thus, the tested vapor space thicknesses are selected as 2 mm, 3 mm and 6 mm for experimentation. The top frames are manufactured of acrylic plates. The depth between the grooved frame and top frame is 6 mm. Therefore, h_v which is shown in Fig. 2.10 is arranged for each different vapor space thickness.

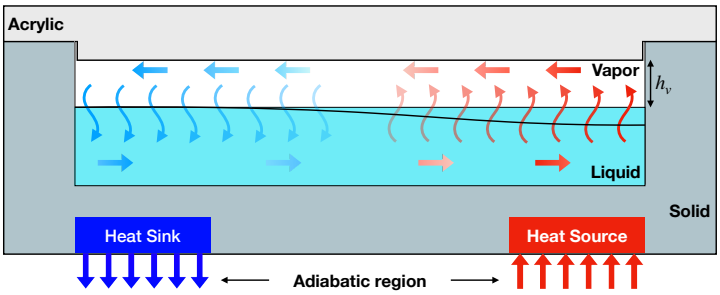

Figure 2.10: FGHP schematic showing the vapor space thickness

HP performance highly depends on the amount of working fluid along the grooves. In order to measure the fluid volume inside FGHP, the liquid level is recorded using a caliper. It is observed that elevation measurements, conducted before increasing the heat load for each experiment, lead to changes in the working fluid propagation along the FGHP. An example of the measurements performed on the $h_v = 2$ mm FGHP is given in Table 2.3.

This variation negatively affects evaluating the same filling ratio at different heat inputs. In addition to this, the small gap also creates a capillary structure leading to trapping some amount of working fluid in there. Consequently, changing the orientation of the heat pipe to measure the elevation induces the trapped liquid to displace from the gap. Also, this trapped liquid also forms during the experimentation which hinders measuring the actual amount of working fluid that places on the grooved frame. The effective filling ratio is more significant which could not be measured in

the present experimental setup. Therefore, it is decided to continue the experiments without measuring the filling ratio.

Table 2.3: Elevation of working fluid measurements at different filling ratios experimented on FGHP with $h_v = 2\ \mathrm{mm}$

	Measured elevation [mm]	
Q_{in} [W]	FR A	FR B
2	18	16
4	15	14
7	12	10

Experiments start at fully flooded condition. Without any inflow or outflow of working fluid to the heat pipe system, different heat rates are tested. Subsequently, the working fluid inside the FGHP is vacuumed for a duration of 15–20 seconds to obtain different filling ratios which are experimented with at each heat rate. This process is repeated until there is no remaining working fluid inside the heat pipe system which refers to the dry case. In this study, since the filling ratio could not be measured, different filling ratios are indicated with numbers in brackets such as FR[1], FR[2], FR[3], etc. denoting increasing filling ratios with increasing index.

2.2.4 Silicon FGHP Experiments

HGA was introduced in 2021 [73] aiming to improve capillary pumping and evaporation as introduced in Chapter 1. It was tested on the copper FGHP; however, they could not further decrease groove widths due to the manufacturing limitations of metals. To overcome this, it is proposed to test HGA on the silicon FGHP since manufacturing of the narrower channels is possible with the etching technology. Thereby, the effective thermal conductivity of HP is aimed to be increased. The other advantage of using silicon as a base material is that many electronic devices are made of silicon; therefore, it is possible to integrate HP directly into the heat source of the device.

The goal of the experiments is to test the integrity of the experimental setup with the silicon HP. In this experiment, the silicon wafer and stainless-steel plate are bonded by vacuuming. Therefore, there can be high contact thermal resistance between the silicon wafer and the base steel frame. However, the main aim is to test the effect on the performance characteristics of the HGA which can be assessed by comparing it with the straight-grooved FGHP. Water is used as a working fluid since it is more neutral matter preventing any chemical reactions with the upper plate. Geometrical parameters of FGHP are depicted in Fig. 2.11. The specifications of experiments are given in Table 2.4.

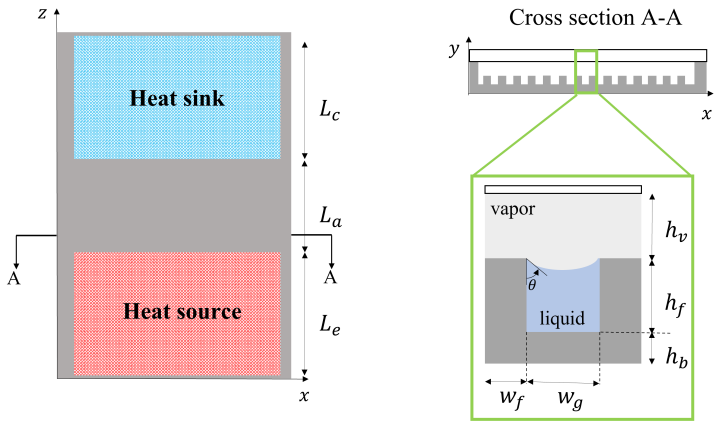

Figure 2.11: Schematics of geometrical parameters of FGHP

Table 2.4: Operating and geometrical specifications Si FGHP experiments

Evaporator length (L_e)	26 mm
Adiabatic region length (L_a)	48 mm
Condenser length(L_c)	26 mm
Fin width (w_f)	0.4 mm
Groove width (w_g)	0.4 mm
Groove height (h_g)	0.4 mm
Vapor spacing (h_v)	5.0 mm
Base height (h_b)	0.6 mm
Number of grooves (N_g)	29

In Fig. 2.12, the measured temperature values at the solid wall are given for different filling ratios operated at the 2 W heat load.

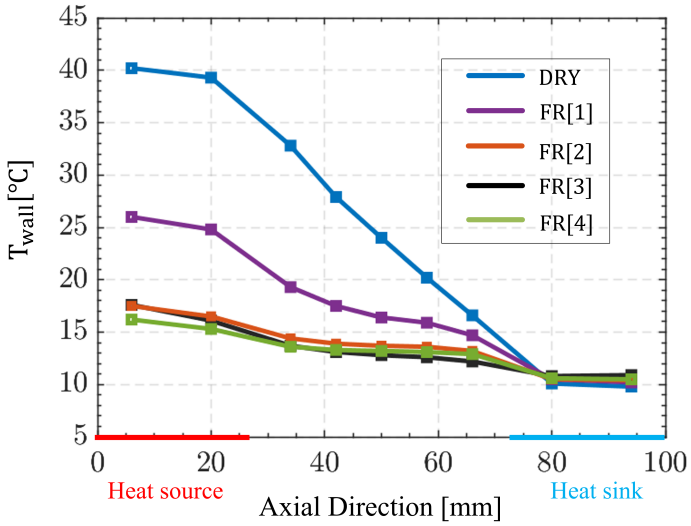

Figure 2.12: Wall temperature variation on Si FGHP for varying filling ratios

The figure shows that the maximum temperature at the wall is measured as 41°C and 16°C for dry and FR[4]. Regarding this reduction in maximum wall temperature, it can be said that the experimental setup can be used for testing FGHP with HGA on the silicon wafers. On the other hand, condensation formed in the top frame is observed when water is used as a working fluid, which is photographed and presented in Fig. 2.13. For further studies, using different working fluids may make it easier to assess the HP performance.

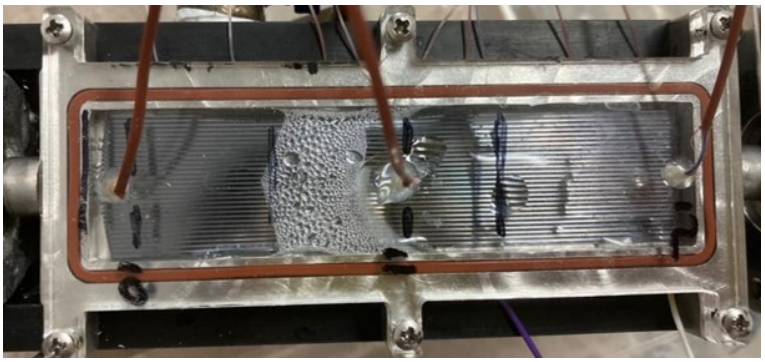

Figure 2.13: Condensation on the top frame

CHAPTER 3

RESULTS

3.1 Numerical Model Validation

In order to validate the present model, it is tested with the FGHP configurations previously studied. The first validation study is performed with the version of the developed model that the vapor flow and interfacial effects were not included. This model, which was already validated [20,73], is used to ensure that the model can operate successfully without losing its accuracy. The second tested configuration is taken from an experimental study conducted by Lips *et al.* [39]. In this study, the radius of curvature measurements was given for different vapor spacing under different heat loads. It is chosen to test the ability to capture the hydrodynamic behavior for varying vapor space thicknesses. In addition, temperature distribution was also presented under a high heat load for a FGHP with a specific vapor spacing.

3.1.1 Validation with the Model without Vapor Flow

The developed model by Saygan *et al.* [20, 73] solves only liquid domain assuming constant vapor pressure and temperature. In order to validate the model, experiments on two different FGHPs were performed under 1.5, 2.1, 2.7 $\mathrm{Wcm^{-2}}$ heat rates. The wall temperature was measured at 15 different points obtaining a good agreement between numerical and experimental results. $\mathrm{HP}\ 600 \times 400$ is selected for validation study since the vapor flow experiments are also conducted on this FGHP configuration in the present study. The operational and geometrical parameters which are shown in Fig. 2.11, are given in Table 3.1 and simulations are performed with 9.5 W heat input.

Table 3.1: Operating and geometrical specifications for validation study [73]

Base material	Copper
Working fluid	IPA
L_e	$26\ \mathrm{mm}$
L_a	$48\ \mathrm{mm}$
L_c	$26\ \mathrm{mm}$
w_g	$0.6\ \mathrm{mm}$
w_f	$0.6\ \mathrm{mm}$
h_g	$0.4\ \mathrm{mm}$
h_v	$6.0\ \mathrm{mm}$
h_b	$1.6\ \mathrm{mm}$
N_g	19

Since this model does not include the vapor flow and the interactions, vapor spacing thickness is not an input of the model. As the vapor space thickness becomes thicker, it is expected that the vapor flow and the interfacial effects on the liquid flow will decrease. Therefore, each FGHP configuration has a limiting vapor spacing thickness in which these effects are no longer effective on the hydrodynamic and thermal performances of FGHP. Thus, a study is performed to investigate on the limiting thickness of tested FGHP. The radius of curvature and wall temperature distributions obtained from the model and present study are compared in Fig. 3.1.

In Fig. 3.1a, radius of curvature, $R(z)$, and edge angle, $\theta(z)$, distribution along the FGHP are presented. The red line which stands for $h_v = 15\ \mathrm{mm}$ and $R(z)$ results obtained by [73] are overlapped with each other. Besides, the yellow dashed line representing the actual vapor space thickness, $h_v = 6\ \mathrm{mm}$, shows a deviation at the condenser section. It is found that the limiting vapor spacing thickness of the current FGHP configuration is $15\ \mathrm{mm}$ according to the model in terms of hydrodynamic behavior.

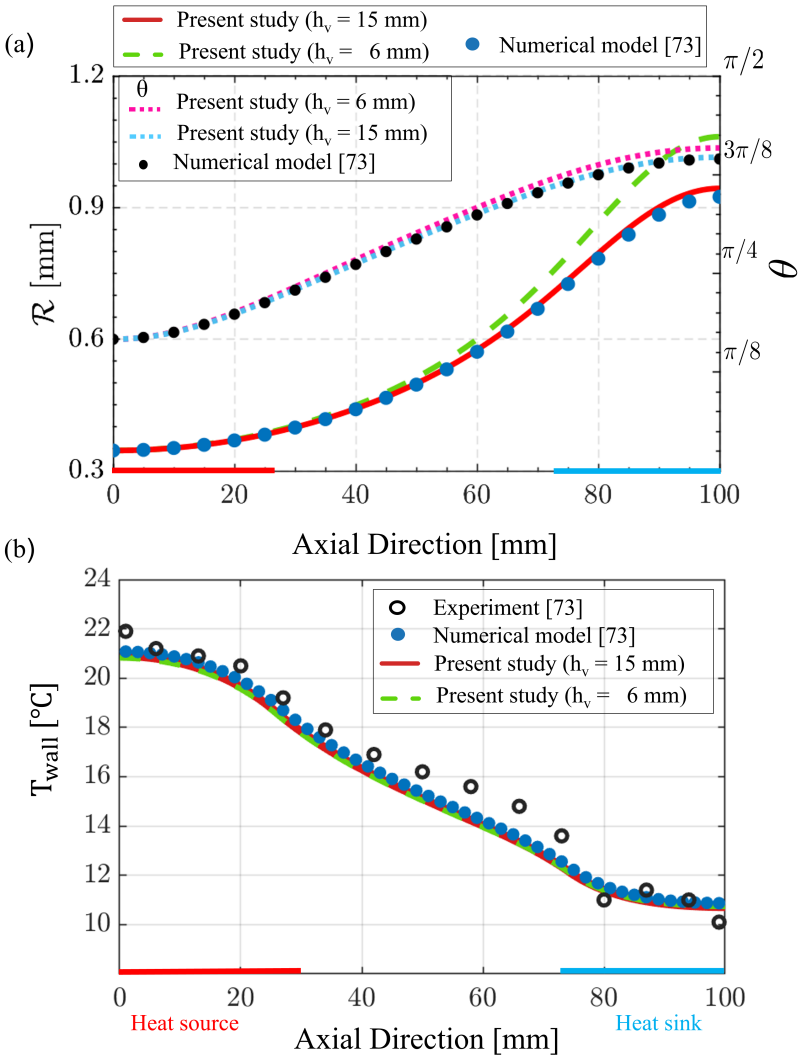

Figure 3.1: Validation with the model that excludes the gas flow effect at 9.5 W heat load [73]: (a) radius of curvature distribution, (b) wall temperature distribution

In Fig. 3.1b, the calculated and experimental temperature distribution results are presented. As seen from this figure, numerical results of wall temperatures for both 6 mm and 15 mm are very close to experimental measurements. Therefore, the current model for $h_v = 6$ mm can also be validated with the experimental data. The deviation formed in the $\mathcal{R}(z)$ at the condenser section is not seen in the temperature profile. This can be explained by that θ at the end of the condenser is found as $73.6°$ and $71.5°$ for 6 mm and 15 mm, respectively. This does not create a substantial difference in the calculation of resistances at the condenser. Therefore, the difference

between $6\ \mathrm{mm}$ and $15\ \mathrm{mm}$ in terms of temperature profiles is not observed.

This study shows that the developed model is capable of capturing the FGHP physics when the vapor flow and interfacial interaction effects are negligible.

3.1.2 Validation of the Effect of Vapor Spacing

Lips *et al.* [39] conducted an experimental study on the FGHP to investigate the effects of filling ratio and vapor space on the thermal performance of FGHP. Different vapor spacing thicknesses were tested by changing the nitrile ring numbers between the top plate and the heat pipe frame. By doing so, $h_v = 1,\ 2,\ 5\ \mathrm{mm}$ vapor spacing configurations could be experimented with for various filling ratios and heat loads. Also, the radius of curvature was measured with confocal microscopy. In this study, T_{wall} and $\mathcal{R}$ measurements were not presented for the same experimentation. Instead, they were provided separately for different operating conditions. Experimental details are tabulated in Table 3.2.

Table 3.2: Operational parameters and geometrical specifications [39]

Base material	Copper
Working fluid	n-pentane
L_e	$20\ \mathrm{mm}$
L_a	$40\ \mathrm{mm}$
L_c	$30\ \mathrm{mm}$
w_g	$0.4\ \mathrm{mm}$
w_f	$0.4\ \mathrm{mm}$
h_g	$0.4\ \mathrm{mm}$
h_v	1.0 and $2.0\ \mathrm{mm}$
h_b	$2.6\ \mathrm{mm}$
N_g	88

Firstly, thermal validation is performed on the FGHP with $h_v = 2\ \mathrm{mm}$ under $7.5\ \mathrm{Wcm}^{-2}$ heat rate. Lips *et al.* [39] stated that the saturation temperature, which is based on the temperature value at the middle of the heat pipe, is set to $40^{\circ}\mathrm{C}$. Therefore, the cool-

ing conditions are arranged based on the mid-wall temperature value as the article studied.

In Fig. 3.2, experimental and numerical results of wall temperature distribution are given. The red line represents current model results, while the blue dots refer to experimental data measured by [39].

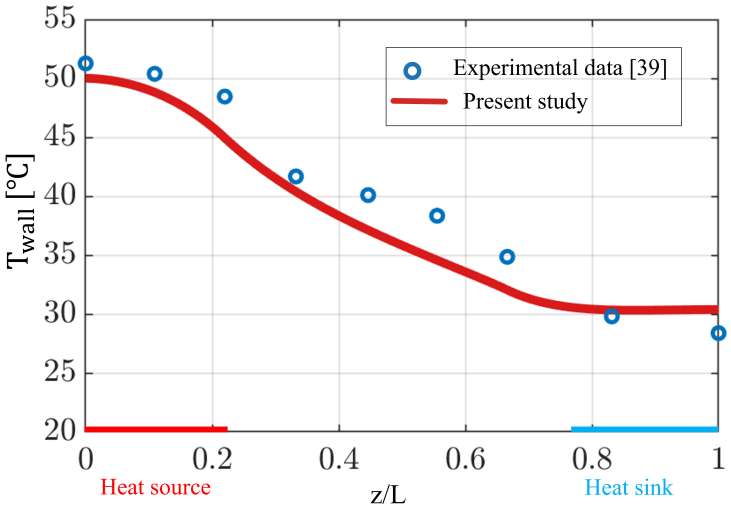

Figure 3.2: Temperature distribution under 7.5 $\mathrm{Wcm^{-2}}$ heat rate for $h_v = 2$ mm

The figure shows that model can predict the trend of temperature distribution on the FGHP wall. The model calculates the temperatures at the ends of the FGHP with a deviation of $1.3°\mathrm{C}$ and $2.0°\mathrm{C}$ from the experimental data which correspond to 5.5% and 8.7% error calculated based on the ΔT_{max}. In addition to that, the thermal analysis of the current model underestimates the temperatures for the adiabatic section. This behavior also shows itself in Fig. 3.1b. According to the model predictions, heat transfer by conduction is more effective in the adiabatic region compared to heat transfer with phase change since the solid line seems linear. However, it differs from the experimental data, where the effects of evaporation and condensation still play an important role in the adiabatic section. In the developed model, phase change physics is also accounted for in the adiabatic section; however, the reason for this variation on the temperature profile at the adiabatic section can be the 4th order polynomial approach for condensation at the fin top. This approach may not give an accurate representation of film thickness variation at the top of the fins, particularly in the transition between

evaporation and condensation, which may not be captured with sufficient accuracy.

In Fig. 3.3, the radius of curvature measurements at the different points of the FGHP and present model result of $\mathcal{R}(z)$ for $h_v = 1,\ 2$ mm are compared at $2.0,\ 3.2$ Wcm^{-2} heat rates, separately to validate the hydrodynamic model. Lips *et al.* [39] used a confocal microscope and optical sensor light to measure the interface geometry. It was stated that the accuracy of the optical sensor measure is lower than 1 μm in both coordinates for calculating the meniscus radius. Similar to the previous one, these simulations are also performed by fixing the mid-point wall temperature to $40°\mathrm{C}$ as proposed by the study.

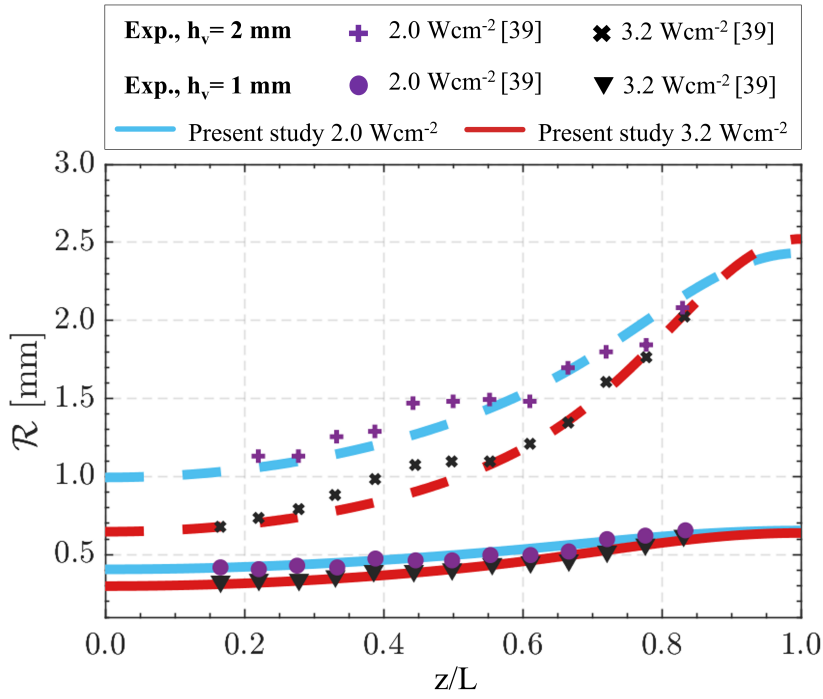

Figure 3.3: Experimental and numerical study comparison for $h_v = 2$ mm and $h_v = 1$ mm (dashed lines represent the numerical results for $h_v = 2$ mm)

The filling ratio is related to the $\mathcal{R}(z)$, since the total volume of liquid within the grooves depends on also the radius of curvature distribution. The experimental data shows that experiments were performed at different filling ratios for $h_v = 1,\ 2\ \mathrm{mm}$ since measurements of $\mathcal{R}(z)$ differ from each other as seen in the figure. Therefore, simulations of current work are arranged in a way that the radius of curvature close to the condenser section is in agreement with the measured data.

Fig. 3.3 shows that the developed model can capture the interface geometry for different vapor spacing and heat loads. The maximum errors for $h_v = 2\ \mathrm{mm}$ simulated with $2.0\ \mathrm{Wcm^{-2}}$ and $3.2\ \mathrm{Wcm^{-2}}$ heat rates are 14.5% and 9% placed at the point $z/L = 0.44$; however, discontinuity is observed at the range between $0.4 \leq z/L \leq 0.6$ in terms of experimental measurement. Also, the mean of the absolute errors of all measured points experimented with $2.0\ \mathrm{Wcm^{-2}}$ and $3.2\ \mathrm{Wcm^{-2}}$ are calculated as 6.1% and 3.1%, respectively.

The error calculations for simulations of $1\ \mathrm{mm}$ vapor space thickness are also performed. The maximum errors of $2.0\ \mathrm{Wcm^{-2}}$ and $3.2\ \mathrm{Wcm^{-2}}$ heat rates are calculated as 16.7% and 9.6%, respectively, while the means of the absolute values of the errors are 8.5% and 4.4%. Therefore, this figure indicates the ability of the model to represent the physics of FGHP for varying vapor space thicknesses.

The mentioned configurations are also simulated with the model in which vapor flow was not included [20]. The radius of curvature results obtained from these models and experimental measurements are presented in Fig. 3.4.

As one can see from Fig. 3.4a, vapor flow strongly affects the meniscus geometry, particularly for the $1\ \mathrm{mm}$ vapor space thickness. For instance, the deviation between the experimental data where $z/L = 0.18$ and the numerical models with and without including the vapor flow are calculated as 0.7% and 20%, respectively for $2.1\ \mathrm{Wcm^{-2}}$, while they are found to be 5% and 13% for $3.2\ \mathrm{Wcm^{-2}}$. Also, the means of the absolute error of the model without the vapor flow are 20% and 12%, which are 8.5% and 4.4% for simulations of the present study $2.0\ \mathrm{Wcm^{-2}}$ and $3.2\ \mathrm{Wcm^{-2}}$ heat rates. This shows that including the vapor flow in the model enhances the accuracy of hydrodynamic results.

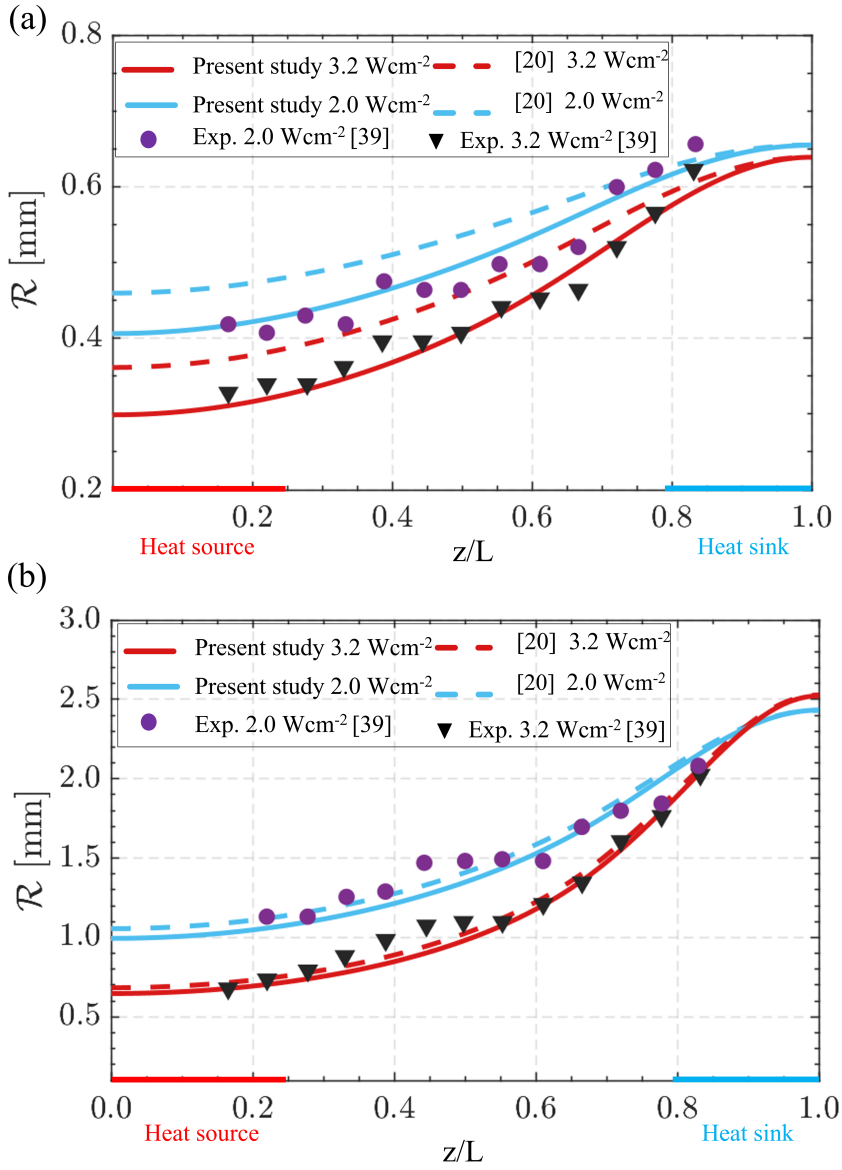

Figure 3.4: Radius of curvature distribution results from the current study, the model developed by Saygan [20] not including the vapor flow (dashed lines), experimental data [39] (a) $h_v = 1$ mm, (b) $h_v = 2$ mm

There is no remarkable difference between the two models for 2 mm vapor space thickness regarding Fig. 3.4b. Thus, 2 mm vapor space thickness may be considered as the limiting thickness for the FGHP configuration in which the vapor flow effects are reduced.

3.2 Simulation Results of Varying Vapor Space Thicknesses

In order to investigate the vapor flow and interfacial effects on the FGHP thermal performance in detail, simulations are performed for $h_v = 1.0,\ 1.5,\ 2.0,\ 5.0 \text{ and } 8.0\,\text{mm}$ on the FGHP configuration experimented by Lips *et al.* [39]. Also, the material contact angle (α_{ca}) between n-pentane and copper was measured 4° [81]. Therefore, it is reasonable to start with $\theta_{beg} = 10^\circ$ to simulations, where α_{beg} is the contact angle corresponding to the beginning of the evaporator. The maximum carrying heat capacity of $h_v = 1\,\text{mm}$ is found $95\,\text{W}$. For the other vapor space thicknesses simulations are arranged such that the edge angle at the end of the FGHP reaches 90°, considering them all simulations are at the edge of the pool formation at the condenser. It corresponds to the beginning of the operating range based on the filling ratio. Similarly, cooling conditions are set to obtain 40°C at the mid-point of the wall.

The edge angle variation along the heat pipe is presented in Fig. 3.5a. It is seen that the contact angle at the evaporator becomes smaller with reduced vapor spacing. This shows that FGHP with $h_v = 1.5,\ 2.0,\ 5.0 \text{ and } 8.0\,\text{mm}$ can work under larger heat loads than the simulated heat input since it does not reach its capillary limit ($\alpha_{beg} \leq \alpha_{ca}$). However, FGHP with $h_v = 1.0\,\text{mm}$ cannot operate at higher heat loads as the contact angle starts very close to the material contact angle. This demonstrates the reduction in the maximum heat-carrying capacity of FGHP.

Also, Fig. 3.5b represents the variation of curvature, κ, –the reciprocal of the radius of curvature– which is linearly proportional to the pressure differences between vapor and liquid phases. Its behavior is consistent with edge angle variation. In other words, it indicates that decreased vapor spacing results in an increased pressure difference toward the evaporator originating from pressure drops in liquid and vapor. The cross-sectional area of the vapor flow depends on the vapor space thickness. As it decreases, the vapor flow accelerates leading to higher shear stress at the interface between liquid and vapor phases. Therefore, it leads to a higher pressure drop in the liquid flow. In addition, the increased vapor flow velocity results in a higher pressure drop in vapor flow which also increases the pressure difference between the two phases.

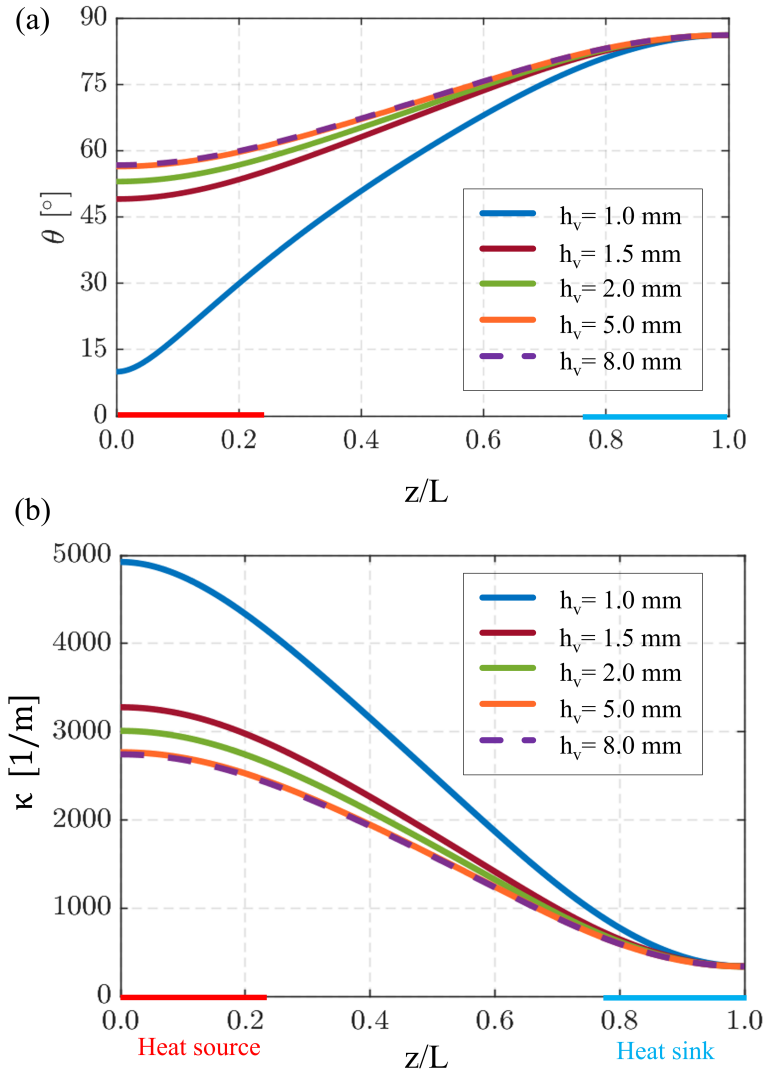

Figure 3.5: (a) Edge angle variation, (b) variation of curvature along the FGHP for varying vapor space thicknesses

The effect of the increased difference between p_ℓ and p_v on the θ is shown with the Young-Laplace equation (see Eq.3.1). As the pressure difference between the two phases increases, the edge angle or contact angle at the evaporator becomes smaller.

$$p_v - p_\ell = \frac{2\sigma}{w_g \cos\theta} \tag{3.1}$$

Fig. 3.6a shows the calculated temperature distribution in the axial direction of FGHP for simulated vapor space thicknesses. FGHP with $h_v = 1$ mm shows a 15% decrease in maximum wall temperature compared with 8 mm vapor space. This can be explained by the variation in the radius of curvature at the evaporator section. When the contact angle decreases, the meniscus radius in the evaporator also reduces. Consequently, the micro-region where the phase change primarily occurs becomes longer, resulting in the expansion of the phase change area. This leads to an increase in heat transfer with phase change by reducing thermal resistance at the evaporator, obtaining better evaporation performance.

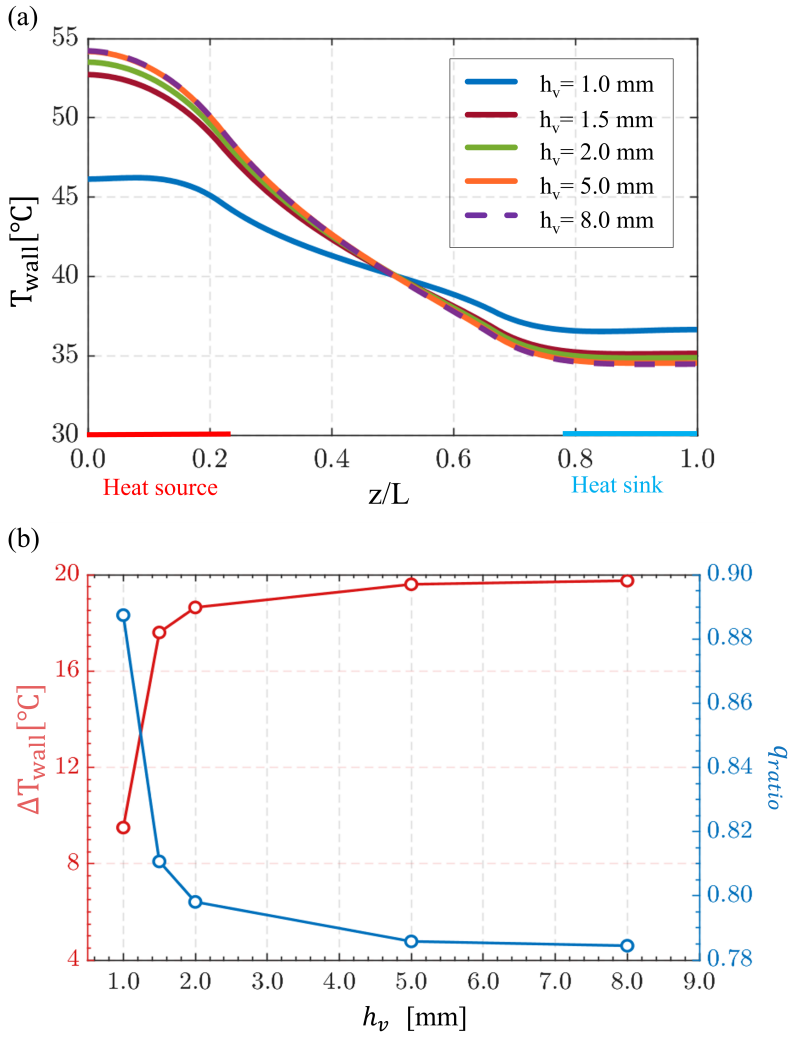

Figure 3.6: (a) Wall temperature distribution, (b) wall temperature difference and q_{ratio}, for varying vapor space thicknesses

Also, the mass flow rate due to evaporation at the thin film region can be written using the equation established by Sujanani *et al.* [82] and enthalpy of evaporation. The thermal resistance corresponding to the phase change of one slice at the fin top $(R^e_{tf,pc})_n$ is calculated using Eq. 3.2 based on these equations [20].

$$(R^e_{tf,pc})_i = \frac{1}{a h_{fg} s_i} \tag{3.2}$$

where s_i, h_{fg} are the arc length of the interface, enthalpy of evaporation and

$$a = \frac{2\hat{\sigma}}{2-\hat{\sigma}} \left(\frac{M}{2\pi R_u T_{\ell v}} \right)^{1/2} \left(\frac{M p_v h_{\ell v}}{R_u T_v T_{\ell v}} \right)$$

where $\hat{\sigma}$, M, $T_{\ell v}$, T_v and R_u are accommodation coefficient, molar weight, liquid-vapor interface temperature, vapor temperature and universal gas constant, respectively. After that, the overall thermal resistance in the film region (R^e_{tf}) is formulated as given in Eq. 3.3 [20].

$$R^e_{tf} = \sum_{i=1}^{p} \left[\frac{1}{(R^e_{tf,\ell})_i + (R^e_{tf,pc})_i} \right]^{-1} \tag{3.3}$$

where $(R^e_{tf,\ell})_i$ is the conduction thermal resistance for liquid film. As one can see from Eq. 3.3, as film becomes thinner, s_i increases, the $(R^e_{tf,pc})_i$ decreases; as well as R^e_{tf}.

Fig. 3.6b represents the wall temperature difference along the heat pipe and the ratio of the heat transferred by phase change to the total heat input, q_{ratio}. It shows that reducing the vapor spacing from $8\ \mathrm{mm}$ to $1\ \mathrm{mm}$ results in a $10^{\circ}\mathrm{C}$ drop in the wall temperature difference. At the same time, a 10% increment in q_{ratio} is observed which means that more heat is transferred by phase change instead of conduction as the vapor spacing is reduced. This result is also in compliance with the drop in the wall temperature difference and demonstrates the evaporation enhancement.

Moreover, Fig. 3.7 shows the shear stress and axial velocity distribution along the FGHP for varying vapor space thicknesses. Since liquid flows from the condenser to the evaporator, the mean velocity of the liquid is in the negative direction.

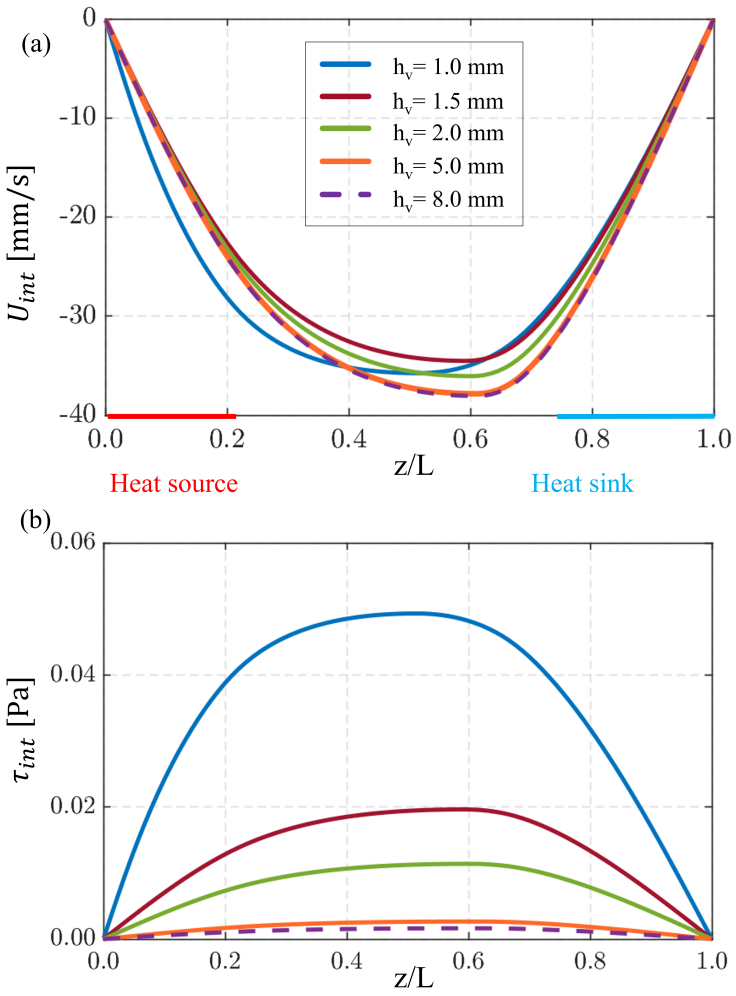

Figure 3.7: Velocity and shear stress distributions at the interface (a) U_{int}, (b) τ_{int}

The blue line represents 1.0 mm vapor space thickness and it shows a higher U_{int} values than the other configurations at the evaporator section. This can also be explained with the evaporation enhancement. Since heat transfer with phase change is increased at the evaporator, the mass flow rate is also increased. Therefore, U_{int} is larger than other vapor space configurations, despite of slowing down effect of the increased τ_{int}. However, as the evaporation enhancement loses its dominance, τ_{int} effect can be more observable. This also shown with the difference between $h_v = 1.5$ mm (yellow line) and $h_v = 5.0$ mm (purple line).

As the vapor space thickness reduces, shear stress at the interface also increases considering Fig. 3.7b. It is seen that for $h_v = 1.0$ mm vapor space thickness, τ_{int} increases nearly 2.5 fold of $h_v = 1.5$ mm at the mid-section of the FGHP. This can be explained by the reduction in the length y– direction although there is a little difference between the U_{int} values for these vapor space thicknesses. This also demonstrates the $\theta(z)$ variation among the varied vapor space thicknesses in Fig. 3.5.

In addition, interface shear, τ_{int} approaches zero, as the vapor space thickness increases. Therefore, it is reasonable to assume symmetrical boundary conditions at the interface between vapor and liquid after a certain value of vapor space thickness. This behavior is also shown in Fig. 3.8. In this figure, velocity contours of the liquid domain are presented at the middle section of FGHP for 1 mm and 5 mm vapor space thicknesses. After obtaining the $p_\ell(z)$ and $\tau_{int}(z)$, the velocity field can be calculated according to the analytical solution given in Ch. 2.

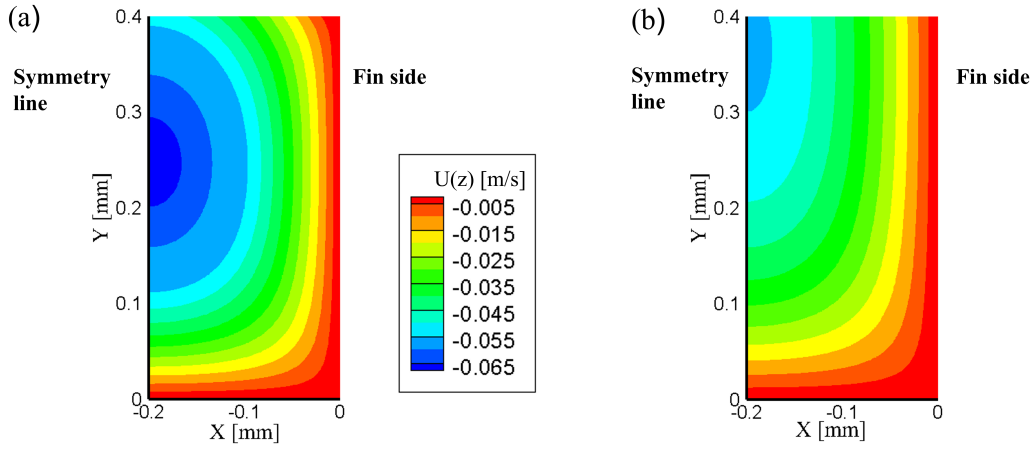

Figure 3.8: Liquid axial velocity contour in x–y plane at middle section of FGHP (a) $h_v = 1$ mm, (b) $h_v = 5$ mm

As seen from Fig. 3.8a, decreased vapor space thickness leads to slow down the liquid velocity due to high $\tau_{int}(z)$. However, the velocity profile is very close to no shear stress at the interface for $h_v = 5$ mm as seen in Fig. 3.8b.

Regarding to Fig. 3.7b, interface velocities at the mid-section of FGHPs with 5 mm and 1 mm vapor space thicknesses are -0.033 m/s and -0.038 m/s, respectively.

These values are consistent with the velocity values shown in Fig. 3.8, where $x = -0.1\,\mathrm{mm}$ and $y = 0.4\,\mathrm{mm}$.

3.3 Vapor Flow Experiment Results

To observe the varying vapor space thickness on the FGHP thermal performance experiments are performed on FGHP with $h_v = 2,\ 3,\ 6\,\mathrm{mm}$. Geometrical parameters of FGHP and operating conditions are given in Table 3.3.

Table 3.3: Operating and geometrical specifications of FGHP configuration for vapor flow experiments

Base material	Copper
Working fluid	IPA
L_e	$26\,\mathrm{mm}$
L_a	$48\,\mathrm{mm}$
L_c	$26\,\mathrm{mm}$
w_g	$0.6\,\mathrm{mm}$
w_f	$0.6\,\mathrm{mm}$
h_g	$0.4\,\mathrm{mm}$
h_v	$2.0,\ 3.0,\ 6.0\,\mathrm{mm}$
h_b	$1.6\,\mathrm{mm}$
N_g	29

Experiments start at the fully flooded state such that the amount of working fluid inside the FGHP spreads at the fin top as well as all over the groove volume. Therefore, a thick film along the groove is formed, which leads to high thermal resistance and reduces the heat transfer with phase change. This makes the conduction heat transfer dominant along the FGHP. When all of the volume between the top frame and the groove frame is filled with liquid, the filling ratios are calculated as 11.5, 16.8 and 32.1 for $2\,\mathrm{mm}$, $3\,\mathrm{mm}$ and $6\,\mathrm{mm}$ vapor space thicknesses, respectively. Also, the filling ratio is zero for dry conditions in all h_v configurations.

The working fluid is vacuumed slowly to test the different filling ratios by the vacuum pump. Two sets are performed for $h_v = 3,\ 6\ \mathrm{mm}$ vapor space thicknesses. In the first set $4.0,\ 5.5,\ 7.0,\ 8.0,\ 9.0$ W heat inputs are experimented, while the other experimental set is operated at $7,\ 9,\ 10,\ 12,\ 13$ W heat loads. After the vacuuming, experiments are performed at all heat inputs of each set. This method is applied for all vapor space configurations. The vacuuming time between the different filling ratios is approximately 10–15 seconds. However, the amount of extracted working fluid is not linear whereas it highly depends on the vacuum pump performance and vacuum hole aperture at the connection to the vacuum line. For example, the top frame behaves as a blockage for vacuuming except for the $6\ \mathrm{mm}$ vapor space. Therefore, the amount of vacuumed liquid shows variation among the configurations.

The wall temperature difference results of the experimental and numerical study are given for $3\ \mathrm{mm}$ vapor space in Fig. 3.9a and 3.9b, respectively. The horizontal axis of Fig. 3.9a shows the different filling ratio (FR), which is not measured as mentioned in the previous chapter. Fully flooded operation refers to [FLOODED], while [DRY] condition is operated without working fluid (only conduction heat transfer takes place). The amount of working fluid inside the FGHP decreases from [FLOODED] to [DRY], which is the direction of the experimentation. Furthermore, the horizontal axis of Fig. 3.9b refers to the simulation input for the contact angle at the beginning of the evaporator. The solid lines depict the results within the operating range. Since the developed model can simulate the onset of dry-out formation, the dashed lines illustrate the behavior after dry-out, based on expected trends rather than obtained from simulations. Additionally, the dotted lines represent simulation results where there is no phase change beyond the point where θ approaches $90°$. As one can see from the figure, the slope changes after passing the operating range which can also be observed from the experimental results.

It is seen that wall temperature differences show a maximum $1°$C variation between the [DRY] and [FLOODED], which is expected since the thermal conductivity of IPA is $0.14\ \mathrm{W(mK)^{-1}}$. In addition, there is no significant difference between FR[7] and FR[8] for all inputs which means that heat transfer with phase change is still not present along the FGHP. Also, this figure shows that the operating range gets narrower with increasing heat input, eventually, it reaches a point corresponding to Q_{max}.

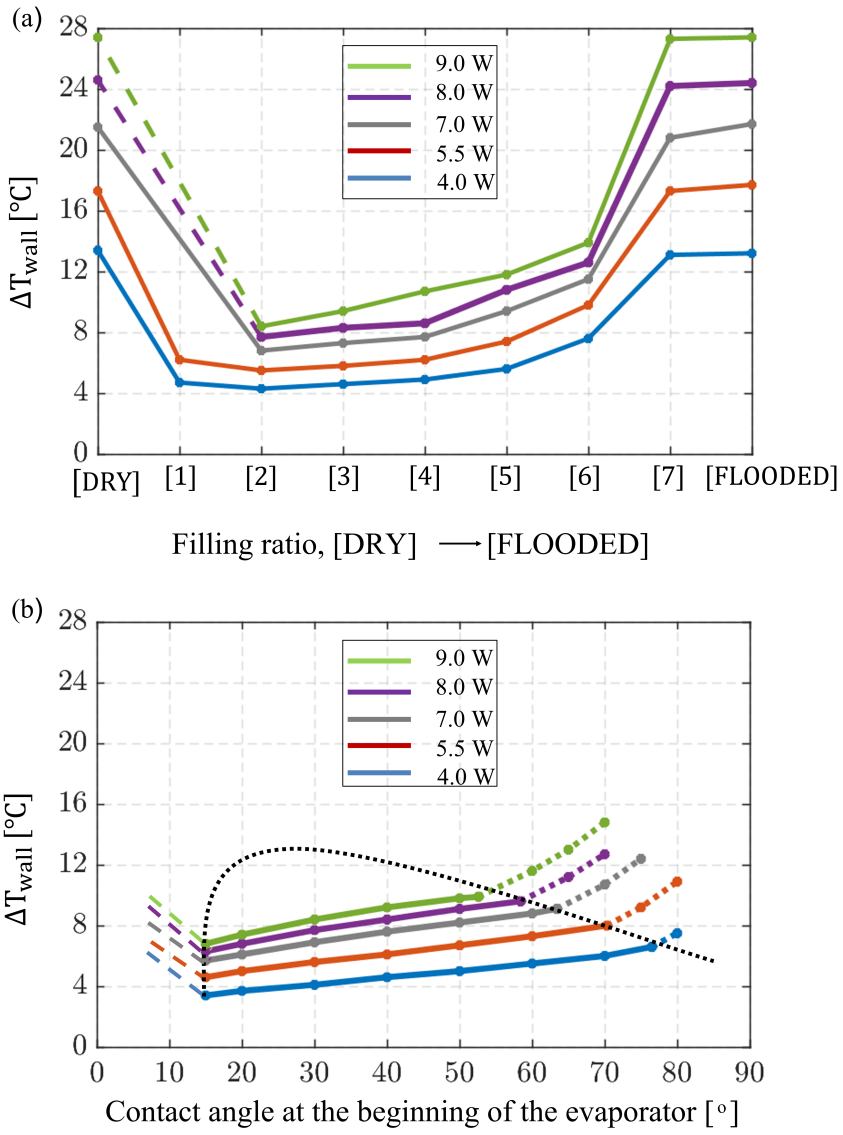

Figure 3.9: ΔT_{wall} results of $h_v = 3$ mm under different heat loads: (a) experimental results for varying filling ratios, (b) numerical results for varying θ_{beg}

According to the simulations, FGHP with FR [5] to FR[2] are in the operating range up to 7 W without any dry-out or pool formation. Furthermore, the operating range becomes narrower with the increased heat input. Eventually, only FR[2] and FR[3] become in the operating range for 9 W. The declining trend in ΔT_{wall} which is also shown numerically with the solid lines in Fig. 3.9b, is captured experimentally. Evaporation enhancement is the main reason for the drop in wall temperature difference

from FR[5] to FR[2]. It can be explained by the formation of a longer micro-region at the evaporator with a decrease in θ_{evap} which is also mentioned in the previous section. Experimental results show that θ_{beg} is decreased up to $15°$. Therefore, it is accepted as $\alpha_{ca} = 15°$ during the operation of FGHP. In addition, the measured and simulated ranges are consistent with each other. To illustrate, simulations give the wall temperature difference between $5.7°\mathrm{C}$ (based on $\theta_{beg} = 15°$) and $9.1°\mathrm{C}$ under the 7 W heat load as the measured limits of the operating range are $5.9°\mathrm{C}$ and 8.7 $°\mathrm{C}$ according to the experimental study.

Horizontal lines of Fig. 3.9a and b are the indicator of the filling ratio. From the simulation aspect, the contact angle at the beginning of the evaporator determines the edge angle distribution as well as the radius of curvature; therefore, each value of θ_{beg} represents different filling ratios. However, it is not possible to determine whether the filling ratio is increased or not by solely considering the θ_{beg} value. Although the amount of working fluid inside the groove volume decreases as the θ_{beg} value decreases, the condensed film thickness at the fin top increases due to the thickening of the film on the fin top with the decreasing edge angle. The schematic of the film thickness with the boundary conditions is given in Fig. 3.10 [83].

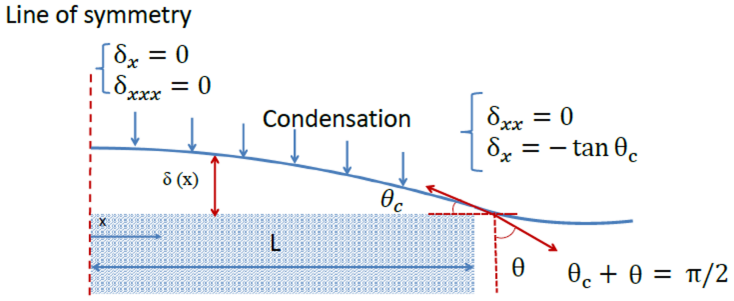

Figure 3.10: Boundary and matching conditions of unidirectional condensation model on the fin top [83]

where $\delta(z)$, θ, θ_c are the film thickness variation, edge angle and complementary angle. As the edge angle decreases at the condenser, the complementary angle increases leading to thicker film thickness at the edge of the fin. This hinders to make the interpretation of the filling ratio value for different θ_{beg} values.

Experimental and numerical wall temperature distribution results for different filling ratios, operated at 7 W heat load, are given in Fig. 3.11. Since FGHP configuration with FR[2]–FR[5] operate within the operating range, their results are compared with the simulation.

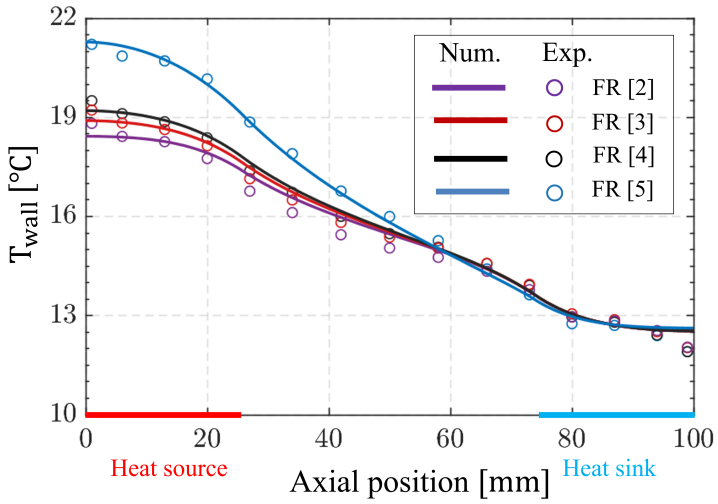

Figure 3.11: Experimental and numerical results of wall temperature distribution for $h_v = 3$ mm at 7.0 W heat load

The figure shows that temperatures corresponding to the condenser section reach 12.5°C showing a similar behavior for each. Since, the flow rate and temperature of the cooling water at the condenser and Q_{in} are kept constant for all four experiments, a similar temperature behavior is expected. However, it is seen that there is an observable temperature difference at the evaporator indicating the different evaporation performance. It is also shown with the simulation results represented with the solid lines in Fig. 3.11 for varying θ_{beg}. It shows that simulations can capture the temperature profile for different evaporation performances. Also, it is seen that the model could not capture the temperatures at the adiabatic region. This discrepancy also repeats itself in the validation study.

After obtaining Fig. 3.11, it is possible to place the experimental data into the simulation results given in Fig. 3.9b. The measured temperatures are found to be the corresponding contact angle at the beginning of the evaporator from the simulations, it is presented in Fig. 3.12.

The figure shows that when the filling ratio is held constant, the initial angle θ_{beg} shows a little variation across the experimented heat inputs, however, it differs for FR[5] under 7 W. Additionally, the figure reveals that α_{ca} falls within the range of $15°$ to $23°$ during the experiments, as indicated by the simulations. In the laboratory, α_{ca} was measured to be between $14°$ and $27°$, which aligns with the numerical values.

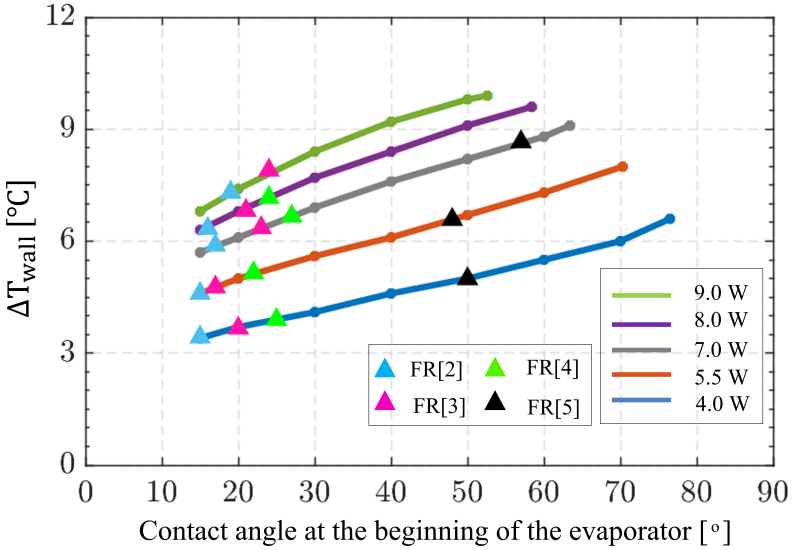

Figure 3.12: Experimental and numerical results of ΔT_{wall} at the operating range of $h_v = 3$ mm FGHP for varying heat inputs

Based on the Fig. 3.9a, measurements could not be performed for FR[1] at $8,\ 9$ W heat inputs (represented with dashed lines), since it dries out slowly and could not reach a steady state almost waiting longer than 2 hours. The photographs given in Fig. 3.13 were taken at certain periods of the experimentation. It shows the expansion of the dry-out region at the evaporator section. As one can see from the figure, the dry-out length expands from 19 mm to 27 mm and 38 mm gradually. The liquid inside the grooves was drawn back to the condenser section by enlarging the dry-out region as time passing. The reason can be that one groove dries up, the temperature in that point increases, and then conduction occurs in the lateral direction and the other groove also dries up eventually. As a result, it prevents the temperature measurements.

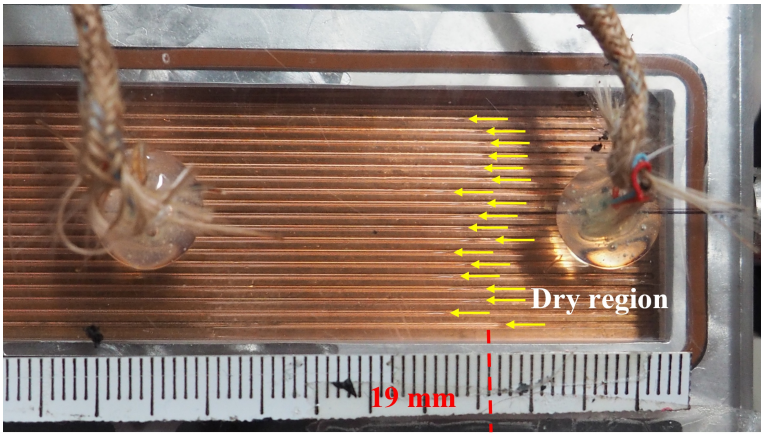

(a) $t = 30$ min

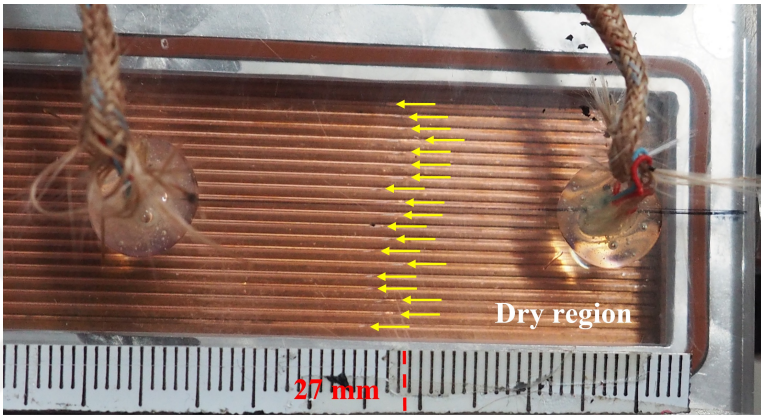

(b) $t = 1$ hour

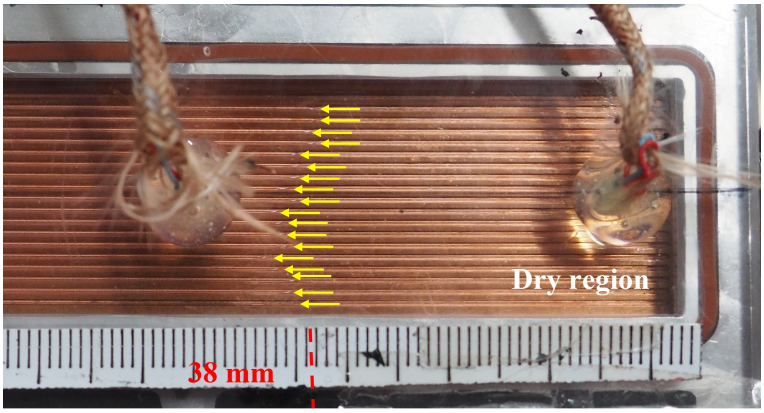

(c) $t = 2$ hours

Figure 3.13: Dry-out region taken at different periods of the experiment: (a) 30 min (dry region is 19 mm), (b) 1 hour (dry region is 27 mm), (c) 2 hours (dry region is 38 mm)

Fig. 3.14 shows the results of wall temperature differences according to the experiments performed on 6 mm vapor space thickness FGHP. Similar behavior with the $h_v = 3$ mm is observed. Figure shows that FR[2] and FR[7] are the operating range for $4.0,\ 5.5,\ 7.0$ W heat inputs, while it is FR[4]–FR[7] for $8,\ 9$ W. However, the results of FR[6] for all heat inputs do not follow the decreasing trend which indicates that there can be release of working fluid during the vacuuming. Also, the reason for the decrease in wall temperature difference for filing ratios between [8]–[10] can be attributed to the FGHP operating as a shorter heat pipe not using its full capacity. Therefore, heat transfer by phase change occurs in that small portion of FGHP resulting in a reduction in ΔT_{wall}.

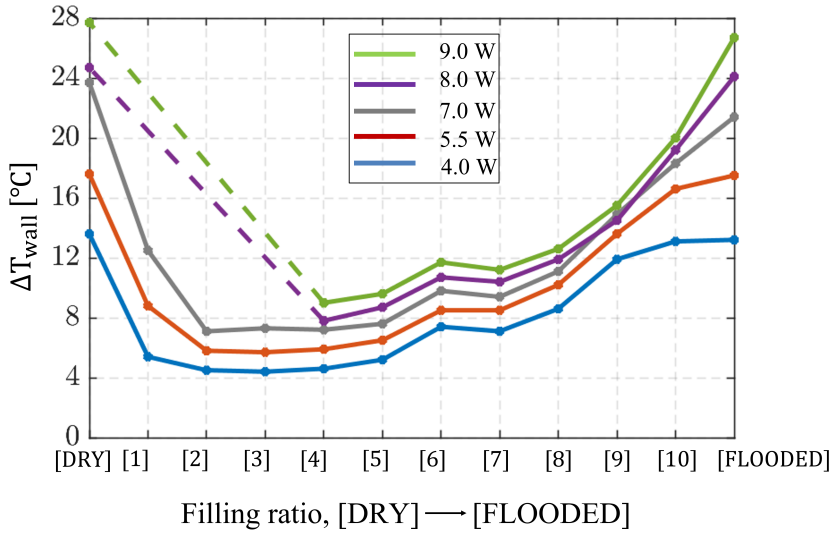

Figure 3.14: Experimental results of ΔT_{wall} for varying filling ratios for $h_v = 6$ mm under different heat inputs

Experimental and numerical results of FGHP configurations with 3 mm and 6 mm vapor space thicknesses are summarized in Table 3.4. Numerical results are based on the simulations in which the contact angle at the beginning of the evaporator starts from $15°$, while the experimental results are noted as measured values at their optimum filling ratio. The table shows that there is a good agreement between the results. When heat input is 9 W, there is 0.6 °C drop in the measured wall temperature difference by decreasing h_v from 6 mm to 3 mm, while it is 0.4°C according to the numerical model. Therefore, it can be said that model can obtain consistent results

with the experimental data for different vapor space thicknesses and heat loads.

Table 3.4: Experimental and numerical model results under different heat loads for $h_v = 3$ mm and $h_v = 6$ mm

ΔT [°C]				
	$h_v = 3$ mm		$h_v = 6$ mm	
Q [W]	Experimental	Numerical	Experimental	Numerical
9	8	7.9	8.6	8.3
8	7.3	7.3	7.4	7.5
7	6.4	6.5	6.8	6.7
5.5	5.1	5.3	5.4	5.3
4	3.9	3.9	4	3.9

Also, the temperature distribution along the FGHP for $h_v = 3$ mm and 6 mm are given in Fig. 3.15 at the $4,\ 7$ and 9 W heat loads. As one can see from the figures, the model can capture the temperature profiles for each heat input and vapor space thickness.

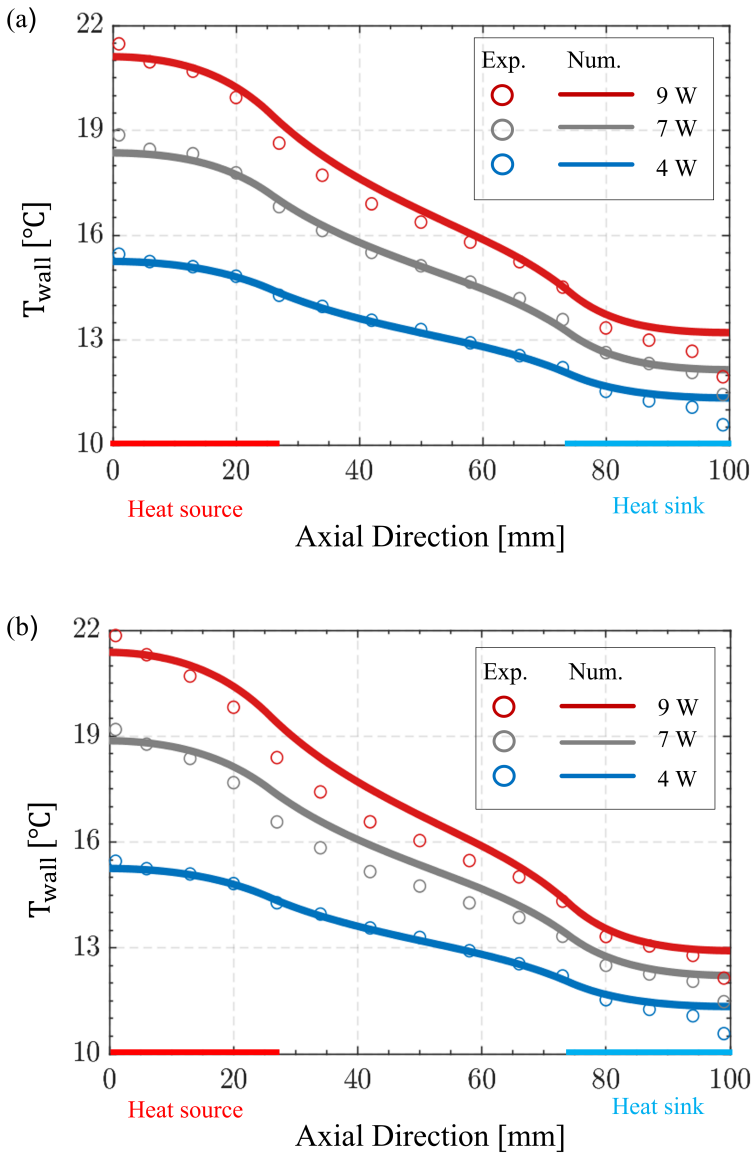

Figure 3.15: T_{wall} variation along the FGHP with $4,\ 7$ and 9 W heat inputs: (a) $h_v = 3$ mm, (b) $h_v = 6$ mm

According to the simulations, Q_{max} is found to be 11 W and 14 W for 3 mm and 6 mm vapor heights, respectively. The reduction in Q_{max} is also studied experimentally which is given in Fig. 3.16. Since the accuracy in Q_{max} calculated from the numerical model is not tested before, different heat inputs with small increments which are $7,\ 9,\ 10,\ 11,\ 12$ and 13 W, are experimented.

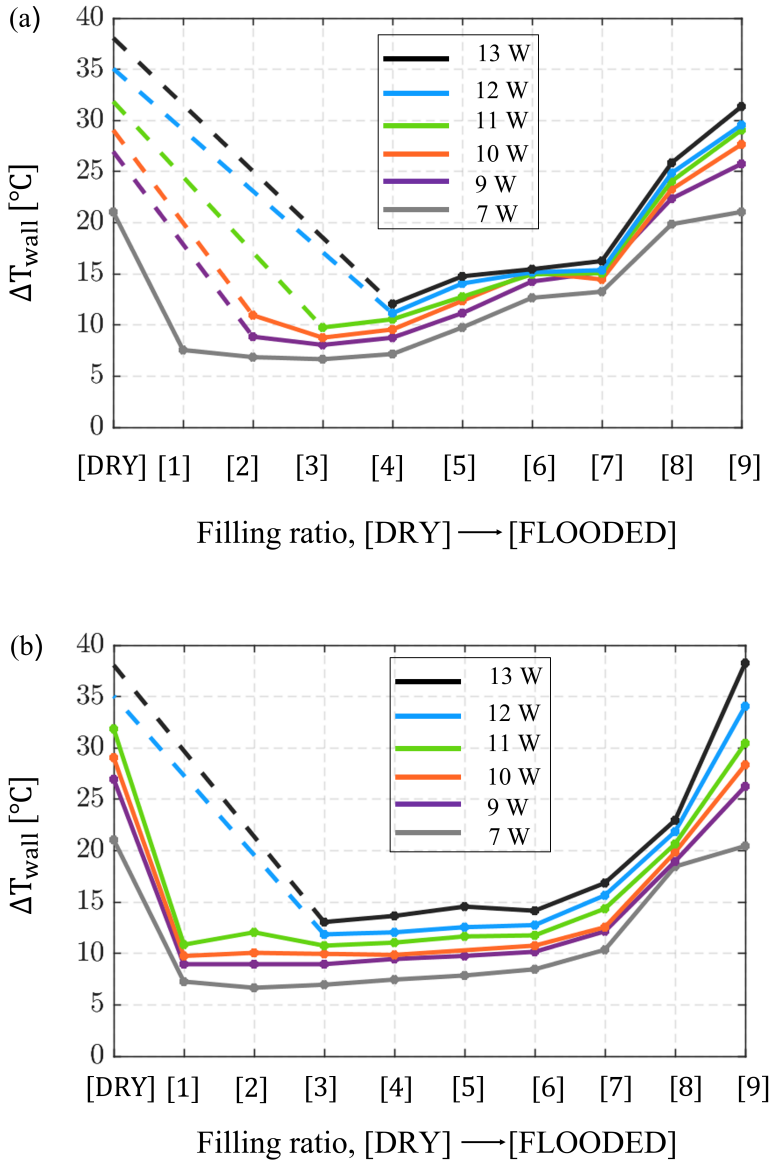

Figure 3.16: Experimental results of ΔT_{wall} with varying filling ratios with 7, 9, 10, 11, 12 and 13 W for: (a) $h_v = 3$ mm, (b) $h_v = 6$ mm

ΔT_{wall} values at the operating range are tabulated in Table 3.5 consisting of both experimental and numerical results for all heat inputs. The lowest numerical result of ΔT_{wall} is simulated with $\theta_{beg} = 15°$.

As seen in Fig. 3.16a, measurement at FR[4], which gives the minimum ΔT_{wall} for 7, 9, 10 and 11 W heat inputs could not be performed with 12, 13 W. Also, the

Table 3.5: Numerical and experimental results of ΔT_{wall} for $h_v = 3$ mm and $h_v = 6$ mm under various heat loads

		Q_{in} [W]					
	h_v	7 W	9 W	10 W	11 W	12 W	13 W
Exp.	3 mm	6.8–7.6	8.1–8.9	8.8–9.6	9.8	11.2	12.1
ΔT_{wall} [°C]	6 mm	6.8–8.5	9.0–10.2	9.8–10.1	10.9–12.1	11.9–12.7	13.1
Num.	3 mm	5.7 –9.1	6.8–9.9	7.1–10.1	9–9.6	-	-
ΔT_{wall} [°C]	6 mm	5.9–10.0	7.3–11.3	7.9–11.7	8.4– 12.0	8.7–12.1	8.8 –11.9

results of the experiments conducted with $7,\ 9,\ 10$ and 11 W heat inputs are within the operating ΔT_{wall} range found from the model. However, there is still a substantial decrease in the wall temperature difference for $12,\ 13$ W heat loads. There are two possible explanations for this behavior and difficult to distinguish. One possibility may be that FGHP operates in a partial dry-out after the heat input 11 W as the measurements for varied FR are decreased seen in Fig. 3.16a. The other possibility can be that the developed model underestimates the Q_{max}. A reason may be the deviation of the kinematic viscosity of IPA with temperature along the heat pipe. Thermophysical properties including kinematic viscosity, are calculated based on the mean vapor temperature value in the model. As the temperature difference along the FGHP increases the variation of thermophysical properties becomes prominent leading to underestimation of Q_{max}. For instance, kinematic viscosity decreases approximately $\%10$ with a temperature increase of $10°$C for IPA.

According to the simulations, the measured ΔT_{wall} values for $h_v = 6$ mm tabulated in Table 3.5 is in the operating range except for 13 W. However, it is not possible to determine the exact Q_{max} value of FGHP with 6 mm vapor space thickness considering the potential omission of a filling ratio in Fig 3.16b. Nevertheless, it can be inferred that the experiments approach Q_{max}.

Furthermore, it shows that FGHP with 3 mm vapor space thickness shows a maximum $1.1°$C reduction in maximum wall temperature difference compared with $h_v = 6$ mm. However, it should be noted that evaporation enhancement with decreased vapor

space thickness, which is found from simulation results, is obtained for the filling ratio at the edge of the pool region. Therefore, the radius of curvature measurements should be performed in order to demonstrate this proposal experimentally, which is not currently available in the laboratory. Also, the study of different vapor flow configurations is expected to continue with $2\ \mathrm{mm}$ vapor space thickness. It is known that the effect of vapor flow becomes more prominent and observable with increased mass flow rates. Consequently, higher heat inputs allow for more apparent observation of the effects of vapor flow. However, FGHP with $h_v = 2\ \mathrm{mm}$ involves a trade-off, namely a reduction in the maximum heat transfer capacity. The decrease in the heat input makes it challenging to capture the vapor flow effects effectively. Moreover, $2\ \mathrm{mm}$ vapor space thickness experiments could not give adequate results due to reasons to be explained in the following section.

3.3.1 Experiments with 2 mm Vapor Space Thickness FGHP

The experiments conducted with $2\ \mathrm{mm}$ vapor space thickness are aimed at investigating the effects of vapor flow in a more pronounced manner. However, robust results could not be obtained from experiments. The major reason is the inability to control the working fluid inside the FGHP.

According to the model, the maximum carrying heat capacity of the configuration is found to be $8\ \mathrm{W}$. In order to be on the safe side, experiments are performed with $4.0,\ 5.5,\ 7.0\ \mathrm{W}$ heat inputs. Fig. 3.17 represents the experimental and numerical results of the wall temperature difference between two ends of FGHP. The corresponding θ_{beg} of experimental ΔT_{wall} is found with the same approach introduced in the previous section.

Fig. 3.17 shows that the obtained lowest contact angle at the beginning of the evaporator is around $40°$. However, lower contact angles, which were obtained for $3,\ 6\ \mathrm{mm}$ FGHP experiments, could not be reached as the vacuuming continues. After that, it starts to dry slowly. At this stage of the experiments, the transient behavior of the configuration differs from the other vapor space thickness configurations. The example of transient behavior is given in Fig 3.18a, while the transient behavior obtained from other configurations is exemplified in Fig 3.18b.

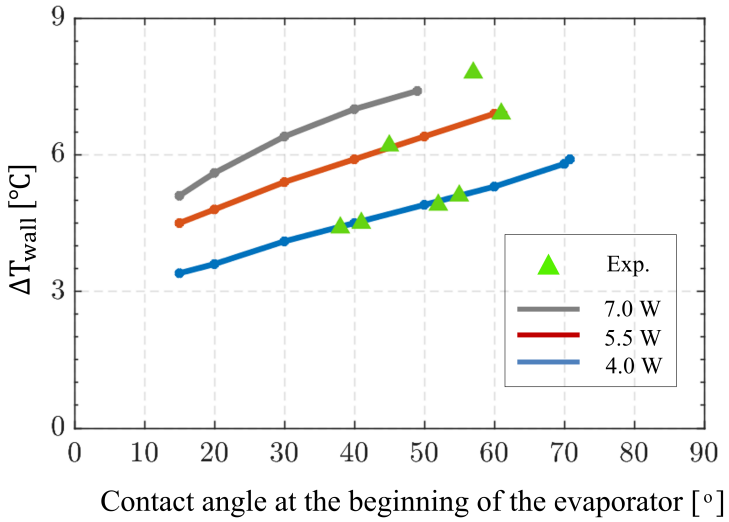

Figure 3.17: Experimental and numerical results of ΔT_{wall} for $h_v = 2$ mm under $4.0,\ 5.5,\ 7.0$ W

The main reason may be the gap between the top frame and the main frame which behaves like a capillary structure such that liquid traps in this gap. The total volume of this gap is $271\ \mathrm{mm}^3$, while the total groove volume is $456\ \mathrm{mm}^3$. According to the observations obtained from $h_v = 2$ mm experiments, the trapped liquid evaporates and condenses constantly resulting in unstable behavior in terms of temperature variation over time during the experiments. Although this gap is also presented for $h_v = 3$ mm configuration, there is a 50% increase in the cross-section area as well as a decrease in the gap volume. Therefore, it makes the effect on the performance becomes more important making it difficult to understand the thermal performance of the FGHP.

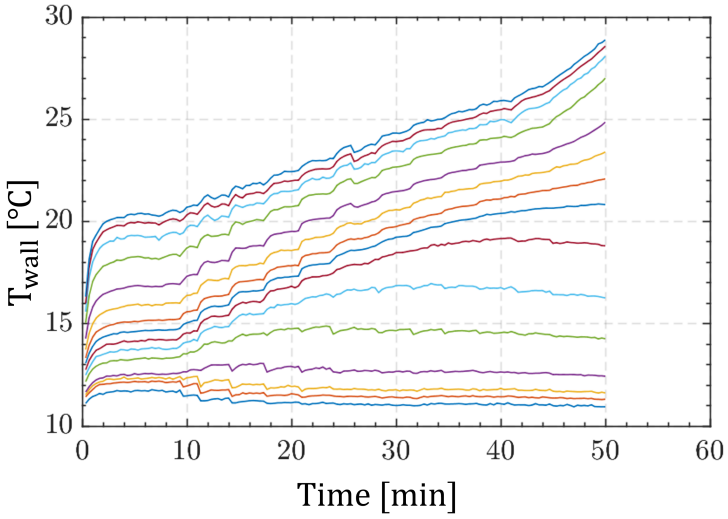

(a)

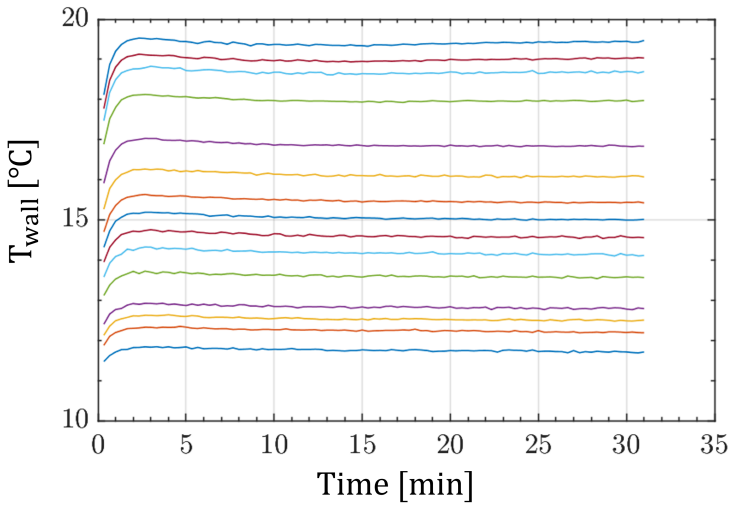

(b)

Figure 3.18: Examples of transient behavior at 7 W heat load for: (a) $h_v = 2$ mm, (b) $h_v = 6$ mm

CHAPTER 4

CONCLUSION

The thesis study examines the effect of vapor flow on the thermal performance of flat-grooved heat pipes by both numerical and experimental analysis. Firstly, a model is developed including vapor flow and interactions between liquid and vapor flows. This model is validated by previous experimental studies. The first validation study is performed with the model which neglects the vapor flow and shear stress at the interface. It shows that including the vapor flow into the model does not deteriorate its accuracy obtaining the same hydrodynamic and thermal behavior for limiting vapor space thickness in which the vapor flow has negligible effect. The experimental and numerical results are in good agreement; however, there is a discrepancy at the adiabatic region which is explained with 4th order polynomial approach for condensation.

The second validation study corresponds to the hydrodynamic validation of the model. It is tested with varying vapor space thicknesses under different heat loads. The model can capture the measured radius of curvature. It shows that the mean error in $\mathcal{R}(z)$ prediction decreases from 12% to 4.4% by including the vapor flow for the lowest vapor space thickness configuration. It is concluded that vapor space thickness should be an input of the model in order to get more accurate results.

A set of simulations are exercised to investigate varying vapor space thickness effects on the thermal performance of FGHP. Results indicate that with reduced vapor spacing, pressure losses in the vapor increase, and pressure variation in the vapor domain results in smaller radii of curvature of the interface in the evaporator. Owing to this, a thinner film micro-region is generated, and the length of the contact line increases. As a result, evaporation is improved in the micro-region, heat transferred by phase change increases, and more uniform temperature distribution on the wall is obtained.

However, increased pressure drop decreases the capillary limit, hence, the maximum heat-carrying capacity of FGHP.

Moreover, different vapor space thicknesses are also experimented with in the modular experimental set-up. The wall temperature differences are obtained at various heat loads and different filling ratios for both $3\ \mathrm{mm}$ and $6\ \mathrm{mm}$ vapor space thicknesses. Evaporation performance is tested numerically and experimentally for $h_v = 3\ \mathrm{mm}$ based on θ_{beg} and different filling ratios, respectively. $\theta(z)$ is considered as different filling ratios and within the operating range of FGHP experimental and numerical $T_{wall}(z)$ are compared, having a good agreement between them. However, the obtained result from the simulation which is the evaporation enhancement with the decreased vapor space thickness is not fully verified due to not obtaining observable measurements. Although experimental results do not contradict with simulation finding, the obtained ΔT_{wall} reduction is not adequate to reach the final conclusion. Also, the radius of curvature should be also measured in order to demonstrate the proposal.

The main findings from the experimental and numerical study are summarized and listed:

- As the heat pipe becomes thinner, vapor flow highly affects the performance of the FGHP. For longer and thinner HPs, viscous loss becomes prominent. It leads to a decrease in the maximum heat-carrying capacity by limiting the capillary pumping pressure of HP.
- FGHP has a limiting vapor space thickness where the interfacial shear stress is very close to zero; therefore, symmetry conditions can be held at the interface line.
- When the FR is close to the flooded case, a little portion of FGHP operates as a heat pipe. Even it does not operate with full performance, it enhances the uniformity of the wall temperature.
- It is observed that with the increased heat input, the operating range becomes narrower, reaching a point for a Q_{max}. However, it is challenging to obtain this point because there can be a part of the FGHP that behaves as a heat pipe by forming the meniscus geometry.
- As the filling ratio decreases, it becomes difficult to reach a steady state, partic-

ularly for high heat inputs. The main reason is that the grooves do not show the same behavior during the experimentation. Therefore, when the dried region of a groove is larger than the others, the adjacent groove also starts dry leading to prolonging the transition state.

All in all, the numerical model is developed and validated. Operation performance and limits are simulated for different vapor flow configurations justifying the physical explanations. Also, different vapor space thicknesses are tested on the experimental setup. Evaporation performance is evaluated for varying filling ratios and heat loads, the model is validated with the experimental work. The numerical model assists researchers in designing heat pipes by assessing their thermal performance based on design criteria. Moreover, the inclusion of vapor flow enhances the comprehensiveness of the model, making it applicable to longer and thinner heat pipes as well. Finally, the aforementioned aspects can be further studied in future research.

- The integrity of the silicon wafer to the modular experimental setup is tested in the current study. However, HGA configurations may be experimented with to test the narrower channels at the evaporator.
- In the present study, the filling ratio is not quantified both numerical and experimental analyses. In the model, 4th order polynomial approach at the condenser leads to the misleading prediction for the filling ratio in the model. From the experimental side, the effective filling ratio could not be measured, since a certain amount of working fluid was trapped in the gap between the top and the main frame. Therefore, the exact filling ratio could not be measured during the experimentation. In addition, filling ratio variation between the different heat loads is observed. Therefore, the control of the fluid may be revised for further studies. In addition, the radius of curvature measurements may be performed in order to assess the hydrodynamic behavior and the effective FR of the FGHP.
- The condensation model for the fin top is quasi-2D which does not mimic the physics precisely, especially in the transition between evaporator and condenser sections. Therefore, a rigorous and comprehensive condensation model may be studied.
- The current model uses the mean of the vapor temperature for thermofluidic

properties along the heat pipe. It can be arranged in a way that properties are temperature-dependent section-wise.

- Evaporation enhancement with the decreased vapor space thickness can be studied on different FGHP configurations with different working fluid types. This proposal is not studied both numerically and experimentally in the literature. It may be studied experimentally by measuring the radius of curvature distribution along the heat pipe.

REFERENCES

[1] A. Inc., "Apple unveils M2 pro and M2 max: Next-generation chips for next-level workflows." Apple Newsroom, January 2023.

[2] V. P. Konyaev, A. A. Marmalyuk, M. A. Ladugin, T. A. Bagaev, M. V. Zverkov, V. V. Krichevsky, A. A. Padalitsa, S. M. Sapozhnikov, and V. A. Simakov, "Laser-diode arrays based on epitaxial integrated heterostructures with increased power and brightness of the pulse emission," *Semiconductors*, vol. 48, pp. 99–103, January 2014.

[3] D. Reay, P. Kew, and R. McGlen, *Chapter 1 - Historical Development*. Oxford: Butterworth-Heinemann, 6th ed., 2014.

[4] B. Zohuri, *Heat Pipe Design and Technology*. Springer International Publishing, 2016.

[5] L. Vasiliev and S. Kakac, eds., *Heat Pipes and Solid Sorption Transformations*. CRC Press, May 2013.

[6] ThermoLab Co. Ltd., "ThermoLab Co. Ltd.." Online, 2009. Accessed: 06.06.2023.

[7] F. Yao, S. Miao, M. Zhang, and Y. Chen, "An experimental study of an anti-gravity vapor chamber with a tree-shaped evaporator," *Applied Thermal Engineering*, vol. 141, pp. 1000–1008, 2018.

[8] T. Xiong, R. Li, Y. Gan, Q. Luo, Y. Li, and R. Qi, "A study on thermal and hydraulic performance of ultra-thin heat pipe with hybrid mesh-groove wick," *e-Prime-Advances in Electrical Engineering, Electronics and Energy*, p. 100117, 2023.

[9] H. Akachi, F. Polasek, and P. Stulc, "Pulsating heat pipes," in *Proc. 5th International Heat Pipe Symposium*, (Melbourne, Australia), pp. 208–217, 1996.

[10] Y. Maydanik, "Loop heat pipes," *Applied Thermal Engineering*, vol. 25, no. 5, pp. 635–657, 2005.

[11] M. Zaghdoudi, S. Maalej, J. Mansouri, and M. Sassi, "Flat miniature heat pipes for electronics cooling: state of the art, experimental and theoretical analysis," *International Journal of Mechanical and Mechatronics Engineering*, vol. 5, no. 3, pp. 714–737, 2011.

[12] B. Lautrup, *Physics of Continuous Matter: Exotic and Everyday Phenomena in the Macroscopic World*. CRC Press, 2nd ed., 2011.

[13] A. Bejan and A. Kraus, *Heat Transfer Handbook*. Heat Transfer Handbook, Wiley, 2003.

[14] H. Alijani, B. Çetin, Y. Akkuş, and Z. Dursunkaya, "Effect of design and operating parameters on the thermal performance of aluminum flat grooved heat pipes," *Applied Thermal Engineering*, vol. 132, pp. 174–187, 2018.

[15] T. P. Cotter, "Principles and prospects for micro heat pipes," 1984.

[16] B. R. Babin, G. P. Peterson, and D. Wu, "Steady-State Modeling and Testing of a Micro Heat Pipe," *Journal of Heat Transfer*, vol. 112, pp. 595–601, 08 1990.

[17] A. Jiao, R. Riegler, H. Ma, and G. Peterson, "Thin film evaporation effect on heat transport capability in a grooved heat pipe," *Microfluidics and Nanofluidics*, vol. 1, pp. 227–233, 2005.

[18] S. J. Kim, J. K. Seo, and K. H. Do, "Analytical and experimental investigation on the operational characteristics and the thermal optimization of a miniature heat pipe with a grooved wick structure," *International Journal of Heat and Mass Transfer*, vol. 46, no. 11, pp. 2051–2063, 2003.

[19] R. Hopkins, A. Faghri, and D. Khrustalev, "Flat miniature heat pipes with micro capillary grooves," *Journal of Heat Transfer*, vol. 121, pp. 102–109, feb 1999.

[20] S. Saygan, Y. Akkuş, Z. Dursunkaya, and B. Çetin, "Fast and predictive heat pipe design and analysis toolbox: H-PAT," *Isı Bilimi ve Tekniği Dergisi*, pp. 141–156, April 2022.

[21] P. S. Ayyaswamy, I. Catton, and D. K. Edwards, "Capillary Flow in Triangular Grooves," *Journal of Applied Mechanics*, vol. 41, pp. 332–336, 06 1974.

[22] B. Suman, S. De, and S. DasGupta, "A model of the capillary limit of a micro heat pipe and prediction of the dry-out length," *International journal of heat and fluid flow*, vol. 26, no. 3, pp. 495–505, 2005.

[23] S. Lips, F. Lefèvre, and J. Bonjour, "Physical mechanisms involved in grooved flat heat pipes: experimental and numerical analyses," *International Journal of Thermal Sciences*, vol. 50, no. 7, pp. 1243–1252, 2011.

[24] G. Schneider, "on-dimensional analysis for the heat transport capability of axially grooved heat pipes including liquid/vapor interaction," in *18th Aerospace Sciences Meeting*, American Institute of Aeronautics and Astronautics, 1980.

[25] K. H. Do, S. J. Kim, and S. V. Garimella, "A mathematical model for analyzing the thermal characteristics of a flat micro heat pipe with a grooved wick," *International Journal of Heat and Mass Transfer*, vol. 51, no. 19-20, pp. 4637–4650, 2008.

[26] D. Khrustalev and A. Faghri, "Thermal Characteristics of Conventional and Flat Miniature Axially Grooved Heat Pipes," *Journal of Heat Transfer*, vol. 117, pp. 1048–1054, 11 1995.

[27] D. Khrustalev and A. Faghri, "Coupled Liquid and Vapor Flow in Miniature Passages With Micro Grooves," *Journal of Heat Transfer*, vol. 121, pp. 729–733, 08 1999.

[28] H. Ma, G. Peterson, and X. Lu, "The influence of vapor-liquid interactions on the liquid pressure drop in triangular microgrooves," *International Journal of Heat and Mass Transfer*, vol. 37, no. 15, pp. 2211–2219, 1994.

[29] E. G. Jung and J. H. Boo, "A numerical study on the heat and mass transfer of a micro heat pipe with a phase-change interface analysis," *Heat and Mass Transfer*, vol. 53, pp. 3363–3372, June 2017.

[30] S. S. Rao and H. Wong, "Heat and mass transfer in polygonal micro heat pipes under small imposed temperature differences," *International Journal of Heat and Mass Transfer*, vol. 89, pp. 1369–1385, 2015.

[31] F. L. Chang and Y. M. Hung, "The coupled effects of working fluid and solid wall on thermal performance of micro heat pipes," *International Journal of Heat and Mass Transfer*, vol. 73, pp. 76–87, 2014.

[32] S. Anand, S. De, and S. Dasgupta, "Experimental and theoretical study of axial dryout point for evaporation from v-shaped microgrooves," *International Journal of Heat and Mass Transfer*, vol. 45, no. 7, pp. 1535–1543, 2002.

[33] F. Lefèvre and M. Lallemand, "Coupled thermal and hydrodynamic models of flat micro heat pipes for the cooling of multiple electronic components," *International Journal of Heat and Mass Transfer*, vol. 49, no. 7, pp. 1375–1383, 2006.

[34] D. Khrustalev and A. Faghri, "Thermal Analysis of a Micro Heat Pipe," *Journal of Heat Transfer*, vol. 116, pp. 189–198, 02 1994.

[35] G. Peterson and H. Ma, "Analysis of countercurrent liquid - vapor interactions and the effect on the liquid friction factor," *Experimental Thermal and Fluid Science*, vol. 12, no. 1, pp. 13–24, 1996.

[36] D. Wu and G. P. Peterson, "Investigation of the transient characteristics of a micro heat pipe," *Journal of Thermophysics and Heat Transfer*, vol. 5, pp. 129–134, April 1991.

[37] E. G. Jung and J. H. Boo, "A numerical modeling for the steady-state performance of a micro heat pipe using thin liquid film theory," *International Journal of Heat and Mass Transfer*, vol. 126, pp. 557–566, 2018.

[38] S. K. Thomas, R. C. Lykins, and K. L. Yerkes, "Fully developed laminar flow in trapezoidal grooves with shear stress at the liquid–vapor interface," *International Journal of Heat and Mass Transfer*, vol. 44, no. 18, pp. 3397–3412, 2001.

[39] S. Lips, F. Lefèvre, and J. Bonjour, "Combined effects of the filling ratio and the vapour space thickness on the performance of a flat plate heat pipe," *International Journal of Heat and Mass Transfer*, vol. 53, pp. 694–702, jan 2010.

[40] S. Kakac, R. K. Shah, and W. Aung, *Handbook of Single-Phase Convective Heat Transfer*. United States: John Wiley and Sons Inc, 1987. [Online].

[41] A. N. Desai, V. K. Singh, and R. N. Patel, "Effect of Geometrical Parameters on the Thermal Performance of Ammonia-Based Trapezoidal-Shaped Axial Grooved Heat Pipe," *Journal of Heat Transfer*, vol. 141, 10 2019. 121801.

[42] S. Zimmermann, R. Dreiling, T. Nguyen-Xuan, and M. Pfitzner, "An advanced conduction based heat pipe model accounting for vapor pressure drop," *International Journal of Heat and Mass Transfer*, vol. 175, p. 121014, 2021.

[43] U. Vadakkan, J. Y. Murthy, and S. V. Garimella, "Transient Analysis of Flat Heat Pipes," vol. 3 of *Heat Transfer Summer Conference*, pp. 507–517, 2003.

[44] C.-K. Huang, C.-Y. Su, and K.-Y. Lee, "The effects of vapor space height on the vapor chamber performance," *Experimental Heat Transfer*, vol. 25, no. 1, pp. 1–11, 2012.

[45] R. Ranjan, J. Y. Murthy, S. V. Garimella, D. H. Altman, and M. T. North, "Modeling and design optimization of ultrathin vapor chambers for high heat flux applications," *IEEE Transactions on Components, Packaging and Manufacturing Technology*, vol. 2, no. 9, pp. 1465–1479, 2012.

[46] K. Baraya, J. A. Weibel, and S. V. Garimella, "Simultaneous wick and fluid selection for the design of minimized-thermal-resistance vapor chambers under different operating conditions," *International Journal of Heat and Mass Transfer*, vol. 136, pp. 842–850, 2019.

[47] Y.-C. Li and S.-C. Wong, "Effects of vapor duct thickness on the capillary blocking and thermal performance of ultra-thin vapor chambers under natural convection cooling," *Applied Thermal Engineering*, vol. 195, p. 117148, 2021.

[48] J. P. Longtin, B. Badran, and F. M. Gerner, "A One-Dimensional Model of a Micro Heat Pipe During Steady-State Operation," *Journal of Heat Transfer*, vol. 116, pp. 709–715, 08 1994.

[49] M. Ivanova, A. Lai, C. Gillot, N. Sillon, C. Schaeffer, F. Lefevre, M. Lallemand, and E. Fournier, "Design, fabrication and test of silicon heat pipes with radial microcapillary grooves," in *Thermal and Thermomechanical Proceedings 10th Intersociety Conference on Phenomena in Electronics Systems, 2006. ITHERM 2006.*, pp. 545–551, 2006.

[50] F. Lefèvre, R. Rullière, G. Pandraud, and M. Lallemand, "Prediction of the temperature field in flat plate heat pipes with micro-grooves – experimental validation," *International Journal of Heat and Mass Transfer*, vol. 51, pp. 4083–4094, jul 2008.

[51] G. P. Peterson, A. B. Duncan, and M. H. Weichold, "Experimental Investigation of Micro Heat Pipes Fabricated in Silicon Wafers," *Journal of Heat Transfer*, vol. 115, pp. 751–756, 08 1993.

[52] C. Gillot, Y. Avenas, N. Cezac, G. Poupon, C. Schaeffer, and E. Fournier, "Silicon heat pipes used as thermal spreaders," *IEEE Transactions on Components and Packaging Technologies*, vol. 26, no. 2, pp. 332–339, 2003.

[53] S.-C. Wong and Y.-C. Lin, "Effect of copper surface wettability on the evaporation performance: Tests in a flat-plate heat pipe with visualization," *International Journal of Heat and Mass Transfer*, vol. 54, no. 17, pp. 3921–3926, 2011.

[54] H. Alijani, B. Çetin, Y. Akkuş, and Z. Dursunkaya, "Experimental thermal performance characterization of flat grooved heat pipes," *Heat Transfer Engineering*, vol. 40, no. 9-10, p. 784 – 793, 2019. Cited by: 20; All Open Access, Green Open Access.

[55] E. G. Jung and J. H. Boo, "A novel transient thermohydraulic model of a micro heat pipe," *International Journal of Heat and Mass Transfer*, vol. 140, pp. 819–827, 2019.

[56] C. Enke, J. B. Júnior, and V. Vlassov, "Transient response of an axially-grooved aluminum-ammonia heat pipe with the presence of non-condensable gas," *Applied Thermal Engineering*, vol. 183, p. 116135, 2021.

[57] K. Baraya, J. A. Weibel, and S. V. Garimella, "Wetting hysteresis as the mechanism of heat pipe post-dryout thermal hysteresis and recovery," *International Journal of Heat and Mass Transfer*, vol. 204, p. 123875, 2023.

[58] L. L. Vasiliev, L. P. Grakovich, M. I. Rabetskii, V. Romanenkov, L. L. Vasiliev Jr, V. Ayel, Y. Bertin, C. Romestant, and J. Hugon, "Grooved heat pipes with a nanoporous deposit in an evaporator," *Heat Pipe Science and Technology, An International Journal*, vol. 1, no. 3, 2010.

[59] J. Min, X. Wu, L. Shen, and F. Gao, "Hydrophilic treatment and performance evaluation of copper finned tube evaporators," *Applied Thermal Engineering*, vol. 31, no. 14-15, pp. 2936–2942, 2011.

[60] M. Singh, N. V. Datla, S. Kondaraju, and S. S. Bahga, "Enhanced thermal performance of micro heat pipes through optimization of wettability gradient," *Applied Thermal Engineering*, vol. 143, pp. 350–357, 2018.

[61] A. A. Abdulshaheed, P. Wang, G. Huang, and C. Li, "High performance copper-water heat pipes with nanoengineered evaporator sections," *International Journal of Heat and Mass Transfer*, vol. 133, pp. 474–486, 2019.

[62] E. C. J. Ng, T. C. Kueh, X. Wang, A. K. Soh, and Y. M. Hung, "Anomalously

enhanced thermal performance of carbon-nanotubes coated micro heat pipes," *Energy*, vol. 214, p. 118909, 2021.

[63] H. Jiang, X. Wang, X. Li, J. Xu, H. Qi, D. Shan, and B. Guo, "Enhanced evaporation performance on a novel microstructured surface with vertical dimension gradient," *International Journal of Heat and Mass Transfer*, vol. 199, p. 123478, 2022.

[64] F. H. Ginting, A. P. Tetuko, N. S. Asri, L. F. Nurdiyansah, E. A. Setiadi, S. Humaidi, and P. Sebayang, "Surface treatment on metal foam wick of a ferrofluid heat pipe," *Surfaces and Interfaces*, vol. 36, p. 102499, 2023.

[65] F. Zhou, G. Zhou, J. Zhou, X. Huai, and Y. Jiang, "A novel ultra-thin vapor chamber with radial-gradient hierarchical wick for high-power electronics cooling," *International Journal of Thermal Sciences*, vol. 183, p. 107896, 2023.

[66] M. Shafahi, V. Bianco, K. Vafai, and O. Manca, "Thermal performance of flat-shaped heat pipes using nanofluids," *International journal of Heat and Mass Transfer*, vol. 53, no. 7-8, pp. 1438–1445, 2010.

[67] Y.-F. Niu, W.-L. Zhao, and Y.-Y. Gong, "Experimental investigation of thermal performance of miniature heat pipe using SiO2-water nanofluids," *Journal of Nanoscience and Nanotechnology*, vol. 15, no. 4, pp. 2932–2938, 2015.

[68] E. Sadeghinezhad, M. Mehrali, M. A. Rosen, A. R. Akhiani, S. T. Latibari, M. Mehrali, and H. S. C. Metselaar, "Experimental investigation of the effect of graphene nanofluids on heat pipe thermal performance," *Applied Thermal Engineering*, vol. 100, pp. 775–787, 2016.

[69] A. Arya, M. Sarafraz, S. Shahmiri, S. Madani, V. Nikkhah, and S. Nakhjavani, "Thermal performance analysis of a flat heat pipe working with carbon nanotube-water nanofluid for cooling of a high heat flux heater," *Heat and Mass Transfer*, vol. 54, pp. 985–997, 2018.

[70] W. Zhao, J. Xu, and J. Li, "Experimental investigation of graphene oxide nanofluids on thermal performance of heat pipe," in *International Conference on Micro/Nanoscale Heat Transfer*, vol. 58905, p. V001T02A003, American Society of Mechanical Engineers, 2019.

[71] E. Sadeghinezhad, A. R. Akhiani, H. S. C. Metselaar, S. T. Latibari, M. Mehrali, and M. Mehrali, "Parametric study on the thermal performance enhancement of

a thermosyphon heat pipe using covalent functionalized graphene nanofluids," *Applied thermal engineering*, vol. 175, p. 115385, 2020.

[72] G. Nagayama, S. Gyotoku, and T. Tsuruta, "Thermal performance of flat micro heat pipe with converging microchannels," *International Journal of Heat and Mass Transfer*, vol. 122, pp. 375–382, 2018.

[73] S. Saygan, Y. Akkus, Z. Dursunkaya, and B. Cetin, "Capillary boosting for enhanced heat pipe performance through bifurcation of grooves: Numerical assessment and experimental validation," *International Communications in Heat and Mass Transfer*, vol. 137, p. 106162, 2022.

[74] P. Chen and Z. Pan, "Heat transfer analysis of flat heat pipe with enhanced microchannel shape," *IEEE Access*, vol. 9, pp. 120833–120843, 2021.

[75] M. Hamidnia, Y. Luo, Z. Li, and X. Wang, "Capillary and thermal performance enhancement of rectangular grooved micro heat pipe with micro pillars," *International Journal of Heat and Mass Transfer*, vol. 153, p. 119581, 2020.

[76] U. Singh and N. K. Gupta, "Stability issues and operating limitations of nanofluid filled heat pipe: A critical review," *Materials Today: Proceedings*, 2023.

[77] P. Mistry, F. Thakkar, S. De, and S. DasGupta, "Experimental validation of a two-dimensional model of the transient and steady-state characteristics of a wicked heat pipe," *Experimental Heat Transfer*, vol. 23, no. 4, pp. 333–348, 2010.

[78] M. H. Elnaggar, M. Abdullah, and M. A. Mujeebu, "Characterization of working fluid in vertically mounted finned u-shape twin heat pipe for electronic cooling," *Energy Conversion and Management*, vol. 62, pp. 31–39, 2012.

[79] Y. Huang and Q. Chen, "A numerical model for transient simulation of porous wicked heat pipes by lattice boltzmann method," *International Journal of Heat and Mass Transfer*, vol. 105, pp. 270–278, 2017.

[80] S. Saygan, *Modeling guided heat pipe design methodology and experimental validation for flat grooved heat pipes*. PhD thesis, Middle East Technical University, 2021.

[81] H.-S. Liang and W.-J. Yang, "Nucleate pool boiling heat transfer in a highly wet-

ting liquid on micro-graphite-fiber composite surfaces," *International journal of heat and mass transfer*, vol. 41, no. 13, pp. 1993–2001, 1998.

[82] M. Sujanani and P. C. Wayner Jr, "Microcomputer-enhanced optical investigation of transport processes with phase change in near-equilibrium thin liquid films," *Journal of Colloid and Interface Science*, vol. 143, no. 2, pp. 472–488, 1991.

[83] M. Alipour, "Modeling of fluid -vapor interface in the condensation zone of a grooved heat pipe," Master's thesis, Middle East Technical University, 2017.